Cell Reports

Article

ALDH1L2 regulation of formate, formyl-methionine, and ROS controls cancer cell migration and metastasis

Graphical abstract

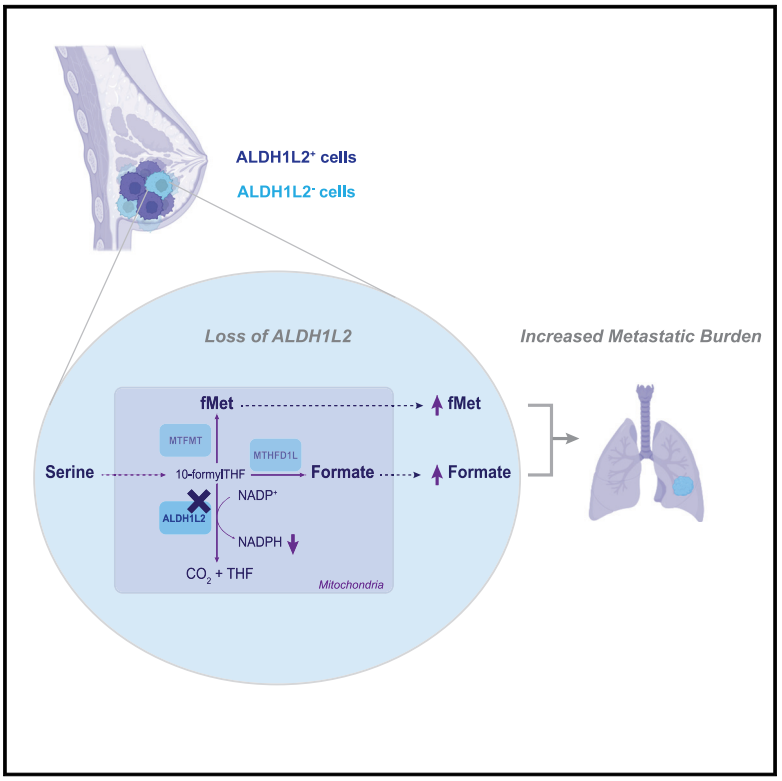

Highlights

- Loss of ALDH1L2 increases formate and formyl-methionine production
- ALDH1L2 levels influence migration in a formyl-peptide receptor-dependent manner
- In the primary tumor, ALDH1L2 levels impact metastatic capacity

Authors

Marc Hennequart, Steven E. Pilley, Christiaan F. Labuschagne, ..., Mariia Yuneva, Charles Swanton, Karen H. Vousden

Correspondence

karen.vousden@crick.ac.uk

In brief

Hennequart et al. describe the role of ALDH1L2, a mitochondrial enzyme involved in one-carbon metabolism, in breast cancer cells. Loss of ALDH1L2 leads to increased production of formate and formyl-methionine, promoting an increase in migration that is dependent on the formyl-peptide receptor and enhancing metastasis *in vivo*.

Hennequart et al., 2023, Cell Reports *42*, 112562
June 27, 2023
https://doi.org/10.1016/j.celrep.2023.112562

CellPress

Cell Reports

CellPress
OPEN ACCESS

Article

ALDH1L2 regulation of formate, formyl-methionine, and ROS controls cancer cell migration and metastasis

Marc Hennequart,[1] Steven E. Pilley,[1] Christiaan F. Labuschagne,[2] Jack Coomes,[1] Loic Mervant,[1] Paul C. Driscoll,[1] Nathalie M. Legrave,[1] Younghwan Lee,[1] Peter Kreuzaler,[1] Benedict Macintyre,[1] Yulia Panina,[1] Julianna Blagih,[3] David Stevenson,[4] Douglas Strathdee,[4] Deborah Schneider-Luftman,[1] Eva Grönroos,[1] Eric C. Cheung,[1] Mariia Yuneva,[1] Charles Swanton,[1] and Karen H. Vousden[1,5,*]

[1]The Francis Crick Institute, 1 Midland Road, London NW1 1AT, UK
[2]Faculty of Natural and Agricultural Sciences, North-West University (Potchefstroom Campus), 11 Hoffman Street, Potchesfstoom 2531, South Africa
[3]Department of Obstetrics-Gynaecology, University of Montreal, Maisonneuve-Rosemont Hospital Research Centre, 5414 Assomption Blvd, Montreal, QC H1T 2M4, Canada
[4]Cancer Research UK Beatson Institute, Glasgow G61 1BD, UK
[5]Lead contact
*Correspondence: karen.vousden@crick.ac.uk
https://doi.org/10.1016/j.celrep.2023.112562

SUMMARY

Mitochondrial 10-formyltetrahydrofolate (10-formyl-THF) is utilized by three mitochondrial enzymes to produce formate for nucleotide synthesis, NADPH for antioxidant defense, and formyl-methionine (fMet) to initiate mitochondrial mRNA translation. One of these enzymes—aldehyde dehydrogenase 1 family member 2 (ALDH1L2)—produces NADPH by catabolizing 10-formyl-THF into CO_2 and THF. Using breast cancer cell lines, we show that reduction of ALDH1L2 expression increases ROS levels and the production of both formate and fMet. Both depletion of ALDH1L2 and direct exposure to formate result in enhanced cancer cell migration that is dependent on the expression of the formyl-peptide receptor (FPR). In various tumor models, increased ALDH1L2 expression lowers formate and fMet accumulation and limits metastatic capacity, while human breast cancer samples show a consistent reduction of ALDH1L2 expression in metastases. Together, our data suggest that loss of ALDH1L2 can support metastatic progression by promoting formate and fMet production, resulting in enhanced FPR-dependent signaling.

INTRODUCTION

The folate cycle contributes one-carbon units for the biosynthesis of nucleotides and methylation reactions.[1] Cancer cells are highly reliant on these pathways,[2,3] as shown by the success of antifolate drugs in the treatment of many types of cancers.[4] An important source of one-carbon units is the metabolism of serine, a non-essential amino acid that can either be taken up from the diet or synthesized *de novo* through the serine synthesis pathway (SSP). The mitochondrial one-carbon metabolism enzymes serine hydroxymethyltransferase 2 (SHMT2) and methylenetetrahydrofolate dehydrogenase 2 (MTHFD2) are upregulated in many types of cancers, including breast cancer,[5,6] and are associated with more aggressive disease.[7,8] Depletion of SHMT2 and MTHFD2 impairs breast cancer growth and reduces breast cancer migration both *in vitro* and *in vivo*.[7,9] Cancer cells satisfy their increased serine requirements by taking up more exogenous serine and upregulating the SSP.[10] In mouse models, tumor growth can be retarded by SSP inhibition, dietary serine and glycine starvation, or a combination of both.[11–16]

10-formyltetrahydrofolate (10-formyl-THF) lies at a crossroad of the mitochondrial one-carbon cycle, serving as a substrate for three mitochondrial enzymes (Figure 1A). MTHFD1 like (MTHFD1L) produces formate—which contributes to the synthesis of purines and deoxythymidine[17,18] but can also be made to excess and excreted from cancer cells.[19] Aldehyde dehydrogenase 1 family member 2 (ALDH1L2) catalyzes the conversion of 10-formyl-THF into CO_2 and THF, providing mitochondrial NADPH that can contribute to antioxidant defense.[20,21] Mitochondrial methionyl-tRNA formyltransferase (MTFMT) uses the formyl group from 10-formyl-THF to formylate methionine-loaded tRNA (fMet-$tRNA^{Met}$), which is used to initiate mitochondrial mRNA translation - resulting in proteins and peptides containing formyl-methionine (fMet).[22,23] Importantly, modulation of serine availability or serine metabolism has been shown to influence redox control[6] and the production of formate and fMet-$tRNA^{Met}$.[19,22]

Recent studies have shown that serine metabolism through the mitochondrial one-carbon cycle plays a role in controlling cancer cell migration and metastasis. For example, *de novo*

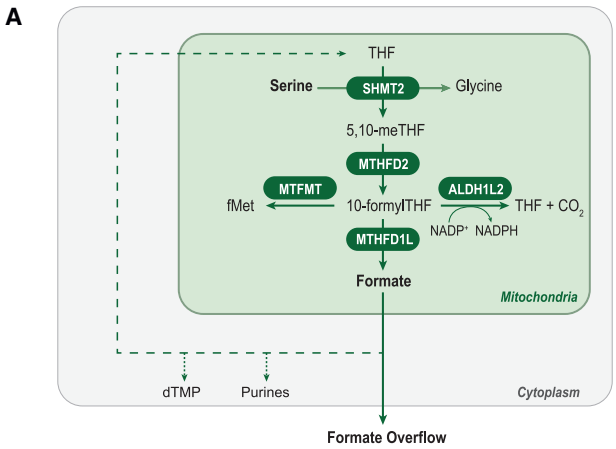

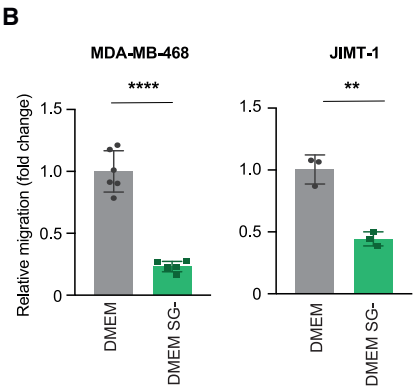

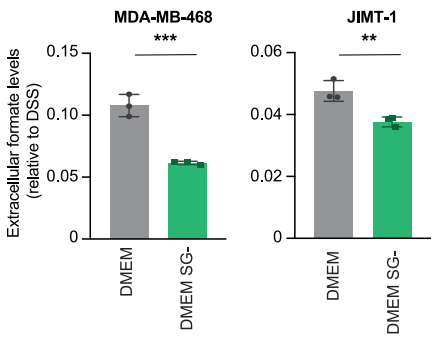

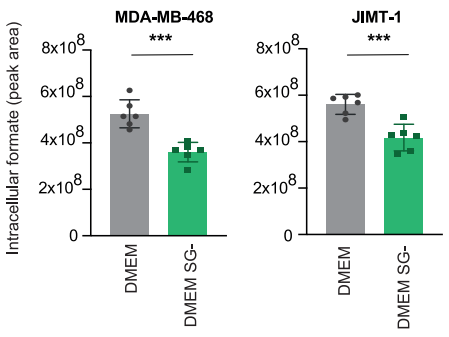

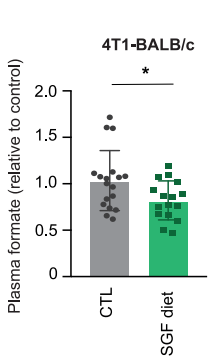

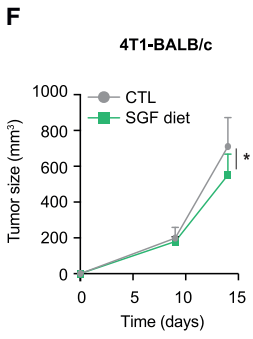

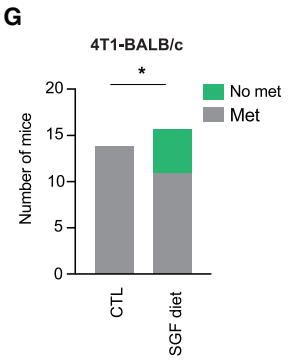

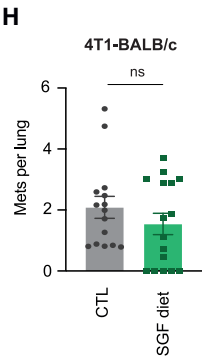

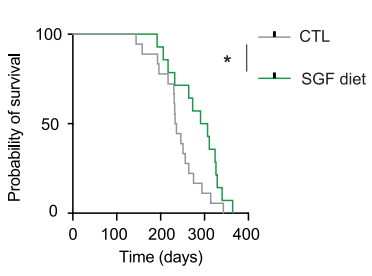

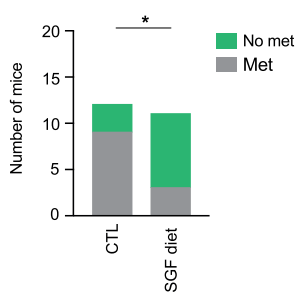

(legend on next page)

serine synthesis induced in response to purine depletion or methotrexate treatment results in increased cancer cell migration.[21,24,25] This response may reflect enhanced formate production, which has been shown to promote migration and invasion of cancer cells.[24,26,27] However, the generation of NADPH and the maintenance of redox defense by one-carbon cycle reactions[28,29] also contribute to the invasive capacity of cancer cells. Reactive oxygen species (ROS) control influences metastatic capacity in several cancer types,[30–34] although enhanced ROS production can either promote or retard metastasis, depending on the model.[35] In this context, ALDH1L2 expression was shown to limit mitochondrial ROS and support metastatic progression of melanoma cells,[30] and a number of studies have suggested that increased ALDH1L2 expression is associated with worse prognosis and reduced disease-free progression.[36–38] In general, however, the link between cancer development and ALDH1L2 expression is relatively unexplored. A role for MTFMT in cancer is also not well established, although changes in mitochondrial protein synthesis and mitochondrial function have clear potential in modulating malignant progression.[39]

In this study, we explored the contribution of products of mitochondrial one-carbon metabolism to cancer cell migration and metastasis, focusing on the role of ALDH1L2.

RESULTS

Serine and glycine starvation reduces cancer cell migration and metastasis

We initially focused on two breast cancer cell lines, MDA-MB-468 and JIMT-1, that were not dependent on extracellular serine and glycine for proliferation (Figure S1A). However, despite maintaining proliferation, serine and glycine starvation significantly decreased the migration of these cells (Figure 1B). Removal of serine and glycine (SG) from the growth medium led to a reduction in both intracellular and extracellular formate production (Figures 1C and 1D) and a reduced NADPH/$NADP^+$ ratio (Figure S1B), consistent with previous observations.[19,40] Although treatment with the antioxidant N-acetyl-cysteine (NAC) did not rescue the migration of SG-starved cells (Figure S1C), it was partially restored by the addition of exogenous formate (Figure S1D). These results suggested that the reduction in migration was not due to lack of antioxidant capacity but may partially reflect lower formate levels.

Using the 4T1 syngeneic transplantable[41–43] and the genetically modified MMTV-MYC[44,45] breast cancer models, we assessed the effect of SG starvation both *in vitro* and *in vivo.* SG depletion led to reduced migration of 4T1 cells *in vitro* (Figure S1E), consistent with our results using the human cell lines. Mice fed an SG-free diet showed reduced levels of SG in the plasma (Figure S1F), accompanied by a decrease in circulating formate (Figure 1E). Mice on an SG-free diet showed a reduction of 4T1 tumor growth (Figure 1F), and there was a reduction of the number of mice that developed lung metastasis (Figure 1G), although there was no significant difference in the number of metastatic lesions per lung (Figure 1H). In a spontaneous model of breast cancer, MMTV-MYC mice fed an SG-free diet showed reduced circulating levels of SG (Figure S1G), improved survival, and a reduction in metastatic burden (Figures 1I and 1J). These results suggest that that a reduction in one-carbon metabolism resulting from decreased exogenous serine availability can lower the ability of cancer cells to migrate and metastasize.

Control of one-carbon metabolism by ALDH1L2

To understand the mechanism by which serine metabolism impacts cancer cell migration, we assessed the consequences of modulating ALDH1L2, which we hypothesized would influence the balance between formate and NADPH production. For these studies, we used human breast cancer cell lines that express

Figure 1. Serine and glycine starvation reduces cancer cell migration and metastasis

(A) Scheme of mitochondrial one-carbon metabolism. Catabolism of serine into glycine by serine hydroxymethyltransferase 2 (SHMT2) transfers one-carbon units onto free tetrahydrofolate (THF) to form 5,10-methylenetetrahydrofolate (5,10-meTHF). 5,10-meTHF is then oxidized by methylenetetrahydrofolate dehydrogenase ($NADP^+$ dependent) 2 (MTHFD2) into 10-formyltetrahydrofolate (10-formyl-THF), which can be further metabolized by 3 different enzymes. The formyl group can be transferred by mitochondrial methionyl-tRNA formyltransferase (MTFMT) onto methionine on tRNA leading to the production of formyl-methionine (fMet) to initiate mitochondrial protein synthesis. 10-formyl-THF can be oxidized into CO_2 by aldehyde dehydrogenase 1 family member L2 (ALDH1L2), releasing THF and reducing $NADP^+$ into NADPH. Finally, 10-formyl-THF can be metabolized into formate by MTHFD1 ($NADP^+$ dependent) like (MTHFD1L), which can either feed into the cytosolic one-carbon cycle, contributing to purine and pyrimidine synthesis, or be excreted into the extracellular space.

(B) Migration of MDA-MB-468 and JIMT-1 cells cultured in DMEM (gray) or DMEM lacking serine and glycine (DMEM SG−, green). Data are shown as mean ± SD of replicate wells, representing 3 independent experiments. Unpaired Welch's t test for MDA-MB-468 and unpaired t test for JIMT-1, $^{**}p < 0.001$, $^{****}p < 0.0001$.

(C) Formate detection by nuclear magnetic resonance (NMR) in the supernatant of cells cultured for 72 h in DMEM (gray) or DMEM SG− (green). Data are shown as mean ± SD of triplicate wells, representing 3 independent experiments. Unpaired t test, $^{**}p < 0.01$, $^{***}p < 0.001$.

(D) Intracellular levels of formate measured by LC-MS in MDA-MB-468 and JIMT-1 cells cultured 72 h in DMEM (gray) or DMEM SG− (green). Data are shown as mean ± SD of triplicate wells pooled from two independent experiments. Unpaired t test,$^{***}p < 0.001$.

(E) Levels of formate relative to control in plasma of 4T1 tumor-bearing BALB/c mice fed a control (CTL; n = 18; gray) or serine/glycine-free (SGF) diet (n = 16; green). Data are shown as mean ± SD of individual mice pooled from two independent experiments. Unpaired t test, $^{*}p < 0.05$.

(F) Growth curve of 4T1 tumor-bearing BALB/c mice fed a CTL (n = 10; gray) or SGF diet (n = 10; green). Data are shown as mean ± SD, representing two independent experiments. Unpaired t test of tumor size at day 15, $^{*}p < 0.05$.

(G) Lung metastasis incidence in 4T1 tumor-bearing BALB/c mice fed a CTL (n = 15; gray) or SGF diet (n = 16; green). The primary tumor was not resected. Pool of two independent experiments. Fisher's exact test, $^{*}p < 0.05$.

(H) H&E quantification of time-matched metastasis per lung, normalized to tumor volume of 4T1 tumor-bearing BALB/c mice fed a CTL (n = 14; gray) or SGF diet (n = 16; green). Pool of two independent experiments. Unpaired t test, p = 0.116.

(I) Probability of survival of MMTV-MYC mice fed a CTL (n = 18; gray) or SGF diet (n = 14; green). Log rank (Mantel-Cox) test, $^{*}p < 0.05$.

(J) Lung metastasis incidence MMTV-MYC mice fed a CTL (n = 12; gray) or SGF diet (n = 11; green). The primary tumor was not resected. Fisher's exact test, $^{*}p < 0.05$.

See also Figure S1.

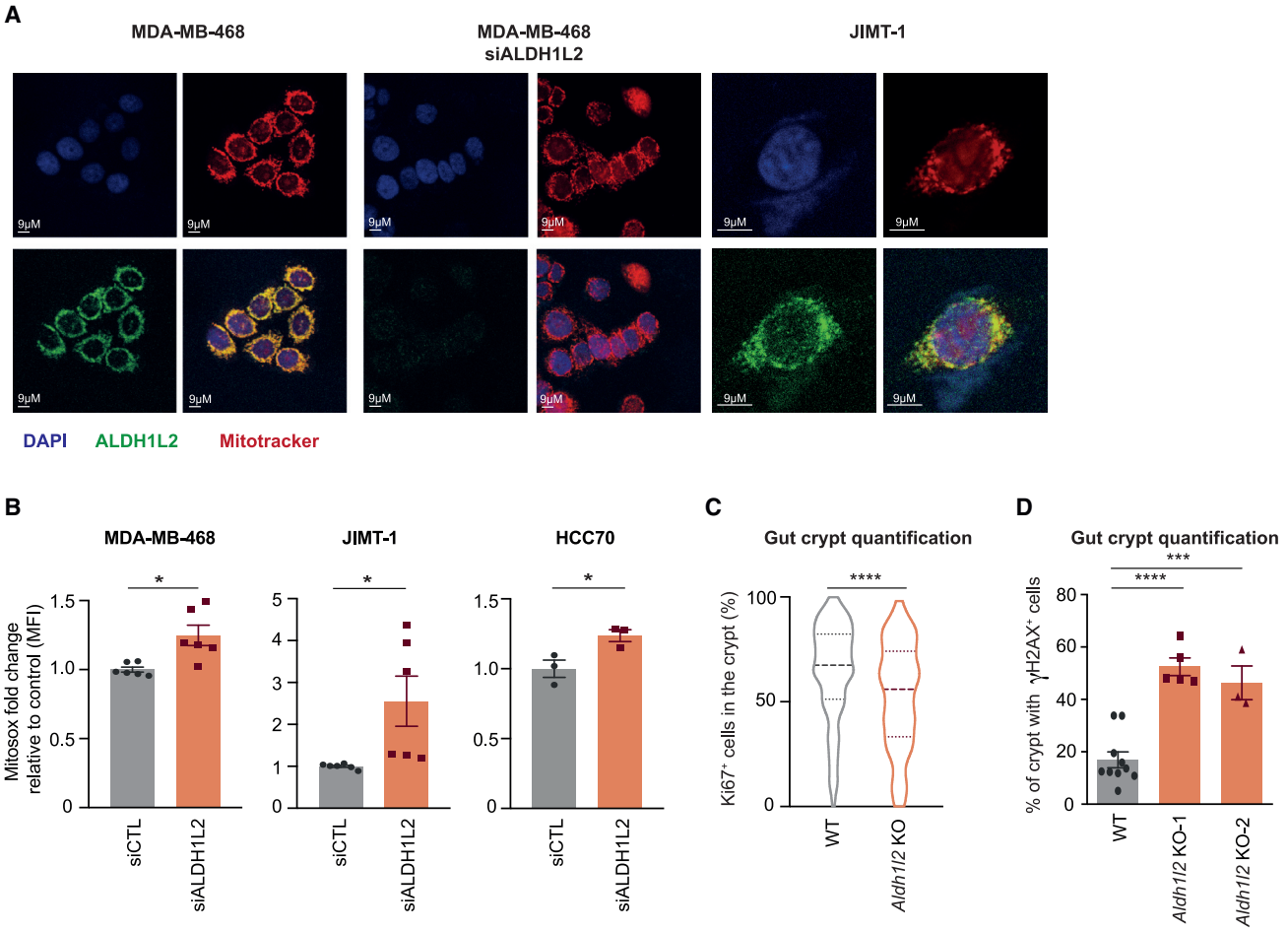

Figure 2. Control of ROS by ALDH1L2

(A) Detection of ALDH1L2 by immunofluorescence of MDA-MB-468 cells transfected for 48 h with non-targeting siRNA or a siRNA targeting ALDH1L2 and JIMT-1 cells. Nuclear staining (blue), ALDH1L2 staining (green), and mitochondrial staining (red) are shown. Scale as indicated.

(B) Fold change relative to control of the mean fluorescence intensity (MFI) of mitoSOX staining measured by flow cytometry in cells transfected with non-targeting siRNA (siCTL; gray) or a pool of siALDH1L2 (orange). Data are shown as mean ± SD of triplicate wells. MDA-MB-468 and JIMT-1 show a pool of two independent experiments. Welch's t test for MDA-MB-468 and JIMT-1, unpaired t test for HCC70, *$p < 0.05$.

(C) Percentage of $Ki67^+$ staining by immunohistochemistry in the intestinal crypt of wild-type (WT; gray; n = 5) or *Aldh1l2* KO mice (orange; n = 5) 72 h after a 10 Gy irradiation. Data are represented as a violin plot of the quantification of 270 crypts across 5 animals per condition. Unpaired Student's t test, ****$p < 0.0001$.

(D) Percentage of $\gamma H2A.X^+$ staining by immunohistochemistry 72 h after 10 Gy irradiation. Data are shown as mean ± SEM of the quantification of at least 50 crypts per mouse per condition (WT n = 10, KO-1 n = 5, KO-2 n = 3), unpaired Student's t test, ****$p < 0.0001$, ***$p < 0.001$.

See also Figure S2.

ALDH1L2 (MDA-MB-468, JIMT-1, and HCC70) and human (MDA-MB-231) and mouse (4T1) breast cancer cell lines with undetectable ALDH1L2 expression (Figure S2A). ALDH1L2 expression was modulated in these lines through small interfering RNA (siRNA) or short hairpin RNA (shRNA) depletion (in MDA-MB-468, JIMT-1, and HCC70) or ectopic expression of ALDH1L2 (in MDA-MB-231 and 4T1) (Figure S2B). As expected, ALDH1L2 protein was localized to the mitochondria in these cells, co-localizing with the mitochondrial dye MitoTracker (Figure 2A). The importance of ALDH1L2 in providing mitochondrial NADPH to limit ROS has been demonstrated in several previous studies.[20,21,30,46] Consistent with these reports, we found that depletion of ALDH1L2 in all three cell lines led to an increase in mitochondrial ROS (Figure 2B), without a change in overall ROS (Figure S2C).

To assess the impact of ALDH1L2 loss *in vivo*, we generated an *Aldh1l2*-deficient mouse, confirming the loss of ALDH1L2 by the lack of protein expression in the pancreas of these mice, where ALDH1L2 levels are normally high[47] (Figures S2D and S2E). Our *Aldh1l2*-null mice were viable and fertile, consistent with a previous report that also described defects in mitochondrial NADPH production in the liver of these mice.[48] To validate the antioxidant role of ALDH1L2 *in vivo*, we initially tested the response of mice to irradiation, where loss of mitochondrial antioxidant function results in a defect in intestinal repair.[49] Consistent with an antioxidant activity for ALDH1L2, *Aldh1l2*

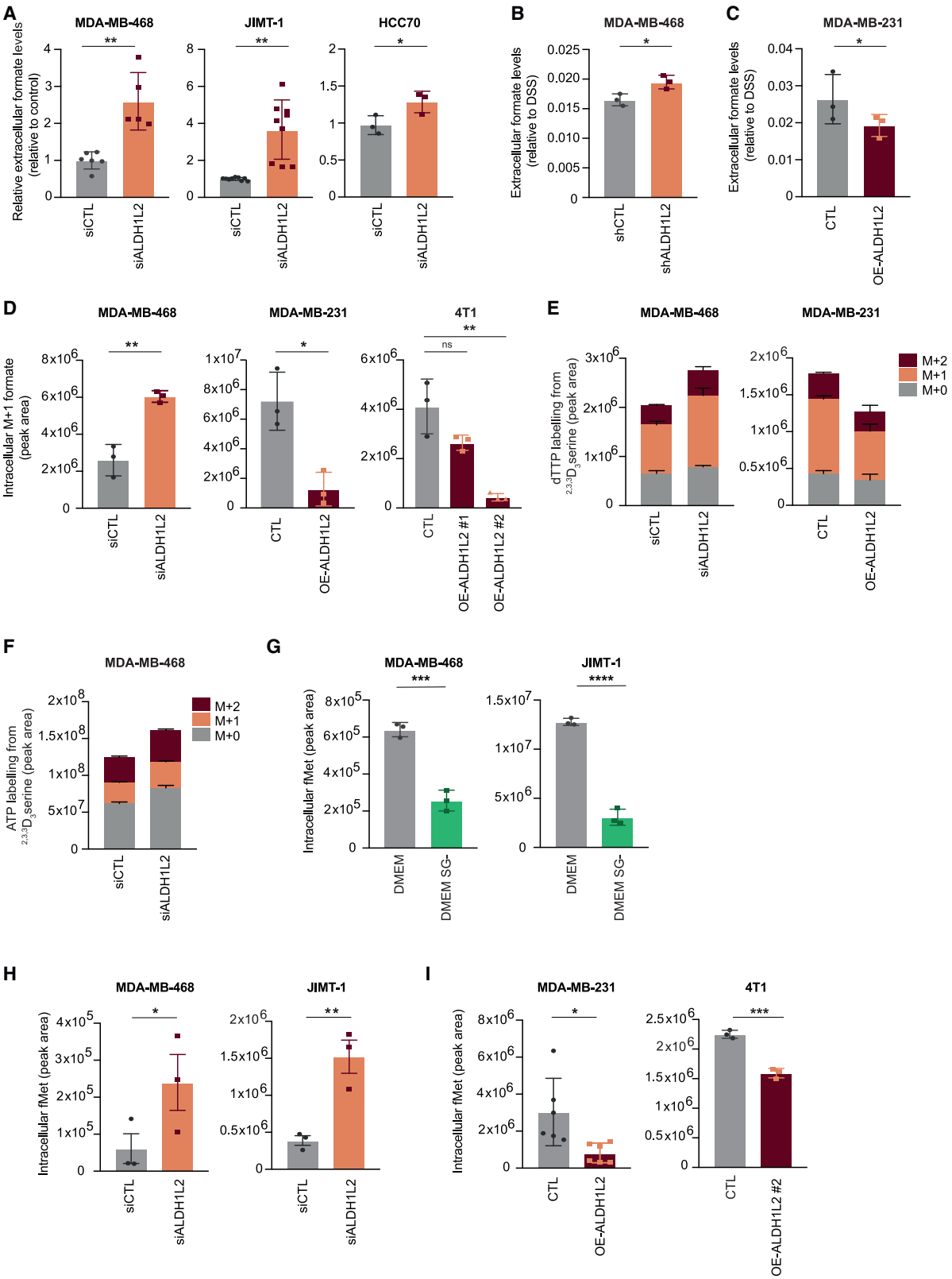

(legend on next page)

knockout (KO) mice showed decreased crypt proliferation, measured by Ki67 staining (Figures 2C and S2F), and retained DNA damage, as shown by an increase in γH2AX-positive crypts (Figure 2D) following irradiation. Taken together, these data confirm a role for ALDH1L2 in limiting mitochondrial ROS in normal and cancer cells.

While the antioxidant role of ALDH1L2 is well established, the possibility that ALDH1L2 activity channels one-carbon units from 10-formyl-THF away from other reactions such as formate or fMet production (Figure 1A) has not been explored. Depletion of ALDH1L2 either by siRNA or shRNA led to an increase in both extracellular and intracellular formate levels (Figures 3A, 3B, and S3A), and overexpression of ALDH1L2 in MDA-MB-231 led to reduced formate overflow (Figure 3C). Using isotope tracing of deuterium-labeled serine, we showed an increase in intracellular levels of the serine-derived m+1 formate following depletion of ALDH1L2 in MDA-MB-468 and a reduction of serine-derived intracellular formate in ALDH1L2-overexpressing MDA-MB-231 and 4T1 cells (Figure 3D). In 4T1 cells, the decrease in formate reflected the level of ALDH1L2 expression (Figure S2B). The changes in the m+1-labeled formate as a percentage of the total formate (Figure S3B) highlighted a clear contribution of serine-derived formate to this pool. These results indicate that ALDH1L2 functions to partition one-carbon units toward NADPH production at the expense of formate production. Using deuterium-labeled serine, as previously described,[50] we demonstrated a slight increase in mitochondrially derived one-carbon units in dTTP (m+1) following ALDH1L2 depletion and decreased labeling of dTTP in ALDH1L2-overexpressing cells (Figures 3E and S3C). m+1 and m+2 labeling of purines was also slightly enhanced upon ALDH1L2 depletion, reflective of the overall formate availability (Figure 3F).

MTFMT is the enzyme responsible for the transfer of the formyl group from 10-formyl-THF to Met-tRNA^{Met}, and we confirmed that depletion of this enzyme resulted in an accompanying decrease in the detection of fMet, indicating a reduction in fMet-tRNA^{Met} levels (Figures S3D–S3F). Lower availability of one-carbon units following SG deprivation resulted in the reduction of intracellular fMet in breast cancer cell lines *in vitro* (Figure 3G) and in the circulation of mice fed an SG-free diet (Figure S3G). ALDH1L2 depletion led to an increase in fMet (Figure 3H), while overexpression of ALDH1L2 cells decreased fMet levels (Figure 3I). Previous work showed that impairment of one-carbon metabolism decreases the abundance of formyl groups available for fMet-tRNA charging, leading to a reduction in mitochondrial protein expression.[22] We found that the higher levels of fMet seen following depletion of ALDH1L2 was accompanied by an increase in expression of the mitochondrial proteins MT-CO2 and ND-1 (Figure S3H), consistent with enhanced mitochondrial mRNA translation. Interestingly, we noted that the addition of exogenous formate also led to increased fMet (Figure S3I), although this effect was weaker than that seen following ALDH1L2 depletion.

Impact of ALDH1L2 modulation on proliferation and migration

Previous studies have identified a role for ALDH1L2 in supporting cancer cell proliferation, an activity that was related to the ability of ALDH1L2 to limit ROS.[20] We also found that depletion of ALDH1L2 decreased proliferation (Figure 4A), a response that was partially rescued by treating cells with either the general antioxidants NAC and glutathione (GSH) or a specific mitochondrial antioxidant, Mito-TEMPO (MTP) (Figure 4B). Interestingly, ALDH1L2 depletion by siRNA or shRNA enhanced the ability of these cells to migrate (Figures 4C, S4A, and S4B) and invade (Figures 4D and S4C), while ALDH1L2 overexpression led to reduced migration (Figures 4E and S4D). In addition, overexpression of ALDH1L2 in a second mouse breast cancer cell

Figure 3. Control of one-carbon metabolism by ALDH1L2

(A) Fold change relative to control of formate levels measured by NMR in the supernatant of cells 72 h after transfection with either non-targeting siRNA (siCTL; gray) or siALDH1L2 (orange). Data are shown as mean ± SD of replicates. MDA-MB-468 and JIMT-1 data are pooled from 2 independent experiments. Unpaired t test, *p < 0.05, **p < 0.01.

(B) Formate levels as measured by NMR in the supernatant of MDA-MB-468 stably transduced with shCTL (gray) or shALDH1L2 (orange) after 72 h in culture. Data shown as mean ± SD of triplicate wells and represent 3 independent experiments. Unpaired t test, *p < 0.05.

(C) Formate levels as measured by NMR in the supernatant of MDA-MB-231 transfected with an empty vector (CTL; gray) or ALDH1L2-overexpressing plasmid (OE-ALDH1L2; burgundy). Data are shown as mean ± SD of triplicate wells and represent of 3 independent experiments. Unpaired t test, *p < 0.05.

(D) Intracellular levels of m+1 formate measured by LC-MS from $^{2,3,3}D_3$ serine in cells 72 h after transfection with either non-targeting siRNA (siCTL; gray), empty vector (CTL; gray), siALDH1L2 (orange), or ALDH1L2-overexpressing plasmid (OE-ALDH1L2; burgundy). Data are shown as mean ± SD of triplicate wells and represent 3 independent experiments. Unpaired t test, *p < 0.05, **p < 0.01.

(E) Mass isotopic distribution of intracellular dTTP measured by LC-MS after 4 h incubation with $^{2,3,3}D_3$ serine of MDA-MB-468 cells transfected with either non-targeting siRNA (siCTL) or siALDH1L2 and MDA-MB-231 transfected with an empty vector (CTL) or ALDH1L2-overexpressing plasmid (OE-ALDH1L2). Data are shown as mean ± SD of triplicate wells and represent 3 independent experiments.

(F) Mass isotopic distribution labeling of intracellular ATP measured by LC-MS after 4 h incubation with $^{2,3,3}D_3$ serine of cells transfected with either non-targeting siRNA (siCTL) or siALDH1L2 for 72 h. Data are shown as mean ± SD of triplicate wells and represent 3 independent experiments.

(G) Intracellular levels of fMet measured by LC-MS in MDA-MB-468 and JIMT-1 cells cultured for 72 h in DMEM (gray) or DMEM SG− (green). Data are shown as mean ± SD of triplicate wells and represent 3 independent experiments. Unpaired t test,***p < 0.001, ****p < 0.0001.

(H) Intracellular levels of fMet in cells 72 h after transfection with either non-targeting siRNA (siCTL; gray) or siALDH1L2 (orange) measured by LC-MS. Data are shown as mean ± SD of triplicate wells and represent 3 independent experiments. Unpaired t test, *p < 0.05, **p < 0.01.

(I) Intracellular levels of fMet as measured by LC-MS in MDA-MB-231 cells 72 h after transfection with either an empty vector (CTL; gray) or an ALDH1L2-overexpressing vector (OE-ALDH1L2; burgundy) or in 4T1 cells stably transduced with either an empty vector (CTL; gray) or an ALDH1L2-overexpressing vector (OE-ALDH1L2; burgundy). Left panel: data are shown as mean ± SD of triplicate wells pooled from 2 independent experiments. Welch's t test, *p < 0.05. Right panel: data are shown as mean ± SD of triplicate wells and represent 3 independent experiments. Unpaired t test, ***p < 0.001.

See also Figure S3.

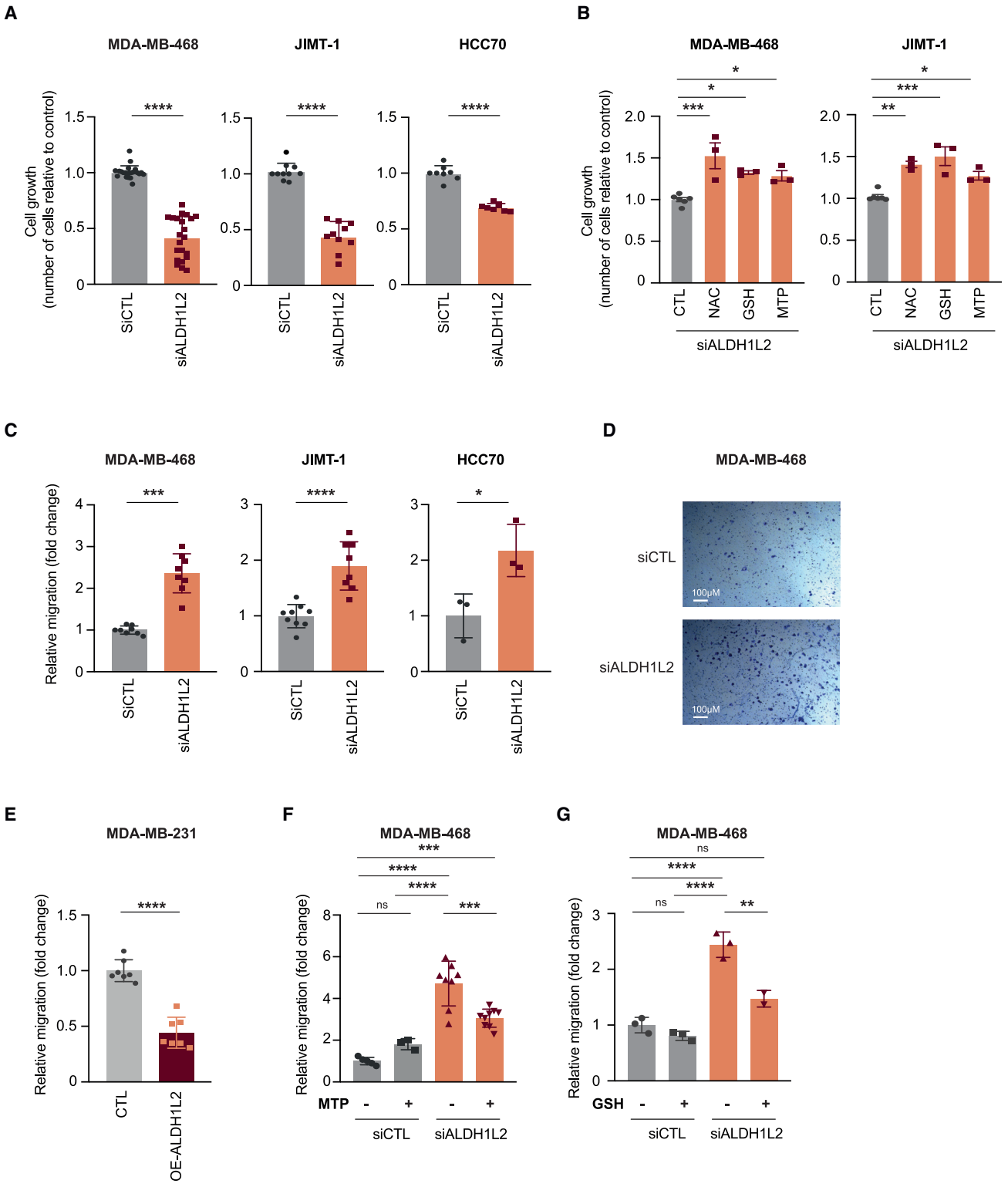

Figure 4. Impact of ALDH1L2 modulation on proliferation and migration

(A) Relative cell number to control of cells transfected for 72 h with either non-targeting siRNA (siCTL; gray) or siALDH1L2 (orange). Data are shown as mean ± SD of replicate wells pooled from 12 independent experiments for MDA-MB-468, 7 independent experiments for JIMT-1, and 5 independent experiments for HCC70. Unpaired Welch's t test for MDA-MB-468 and unpaired t test for JIMT-1 and HCC70, ****p < 0.0001.

(legend continued on next page)

line, E0771, also led to reduced migration (Figures S4E and S4F). Previous studies have shown that in some models, enhanced ROS can promote migration of cancer cells, and we found that treatment of the MDA-MB-468 cells with two different antioxidants partially rescued the increase in migration resulting from depletion of ADLH1L2 (Figures 4F and 4G). These results indicated that the increase in ROS seen following ALDH1L2 depletion in breast cancer cells contributes to—but is not entirely responsible for—decreased proliferation and enhanced migration.

ALDH1L2 depletion promotes migration through FPR1

Previous studies have shown that formate can increase migration of glioblastoma cells,[26,27] and although the mechanism through which formate promotes migration of cancer cells is not well understood, there is a clear role for formylated peptides derived from bacterial or mitochondrial proteins in promoting migration of various immune cells.[51] The formylated peptides derived from these proteins are recognized by the promiscuous G protein-coupled receptors termed formyl-peptide receptors (FPRs), which activate downstream signaling cascades in cells such as neutrophils, macrophages, and epithelial cells to promote migration.[52–55] Interestingly, all our breast cancer cell lines expressed FPR1, one of the three human FPRs (Figure S5A), and treatment of these cells with FPR1 agonists—but not fMet—led to increased migration that was dependent on FPR1 expression (Figures 5A, 5B, and S5B). Depletion of FPR1 from the breast cancer cells (Figure S5C) effectively abrogated the increased migration induced by ALDH1L2 depletion (Figures 5C and 5D). These results show that the migration response to ALDH1L2 depletion is mediated through FPR signaling and indicate that this is in response to increased generation of formylated peptides rather than an increase in fMet itself.

Previous reports have suggested that expression of FPRs correlates with increased invasion in colon and breast cancers.[56,57] Analysis of the MERAV database[58] showed that FPR1 is upregulated in primary breast cancers compared with normal tissue (Figure S5D) and that FPR1 expression was significantly higher in the primary tumors of patients with breast cancer that also had metastases compared with tumors from patients with only localized disease[59] (Figure S5E).

Formate-induced cancer cell migration through FPR1

As shown previously, we found that exogenous formate was able to increase migration of breast cancer cell lines, regardless of ALDH1L2 expression levels (Figure S5F). Interestingly, we found that formate-induced migration of these cells was also dependent on the expression or activity of the FPR (Figures 5E and S5G), consistent with our observation that formate treatment increased fMet production (Figure S3I). The role of the AKT and MAPK pathways in cell migration and invasion is well established,[60,61] and activation of FPR1 in different immune populations and cancer cells has been show to promote increased migration through AKT and MAPK signaling.[62–64] Treatment of MDA-MB-231 cells with formate resulted in an increase in p-AKT, mirroring the same response to two different formate agonists (Figures 5F and S5H), although no change in p-ERK1/2 was detected.

ALDH1L2 contribution to tumor growth and metastasis

TCGA data indicate that while the other mitochondrial one-carbon metabolism enzymes (SHMT2, MTHFD2, MTHFD1L) are significantly upregulated in breast cancers, there is no evidence of consistent overexpression of ALDH1L2 in these tumors (Figure S6A). However, the CCLE data suggested there may be two distinct groups of breast cancers with high and low expression of ALDH1L2 (Figure S6B). This situation is similar to that seen for the SSP enzyme phosphoglycerate dehydrogenase (PHGDH), which is overexpressed in some cancers[11,13] but shows loss of expression in others.[65]

Systemic reduction in SG availability resulted in decreased levels of circulating formate (Figure 1E) and fMet (Figure S3G). Consistent with the ability of ALDH1L2 to lower formate production, we found that whole-body deletion of *Aldh1l2* led to higher levels of circulating formate (Figure 6A), although significant changes in circulating fMet levels were not detected (Figure S6C). Plasma levels of other metabolites such as alanine and lactate remained unaffected (Figure S6D). To assess the effect of ALDH1L2 modulation *in vivo*, we used ALDH1L2-depleted MDA-MB-468 cells. As seen *in vitro*, loss of ALDH1L2 expression did not impact the growth of the tumors arising following injection of the cells into the mammary fat pad of immunodeficient mice (Figure 6B), although the reduction in ALDH1L2 expression

(B) Relative cell number to control of cells transfected for 72 h with siALDH1L2 and treated with 0.5 mM N-acetyl-cysteine (NAC), 2 mM glutathione (GSH), or 50 μM Mito-TEMPO (MTP). Data are shown as mean ± SD of replicate wells and represent 3 independent experiments. Multiple comparison by one-way ANOVA, *p < 0.05, **<0.01, ***p < 0.001.

(C) Migration of cells following transfection with either non-targeting siRNA (siCTL; gray) or siALDH1L2 (orange). Data are shown as mean ± SD of replicate wells pooled from 3 independent experiments for MDA-MB-468 and JIMT-1. Unpaired Welch's t test for MDA-MB-468 and unpaired t test for JIMT-1 and HCC70, *p < 0.05, ***p < 0.001, ****p < 0.0001.

(D) Crystal violet staining of MDA-MB-468 cell invasion after transfection with either non-targeting siRNA (siCTL) or siALDH1L2. Representative of 2 independent experiments with scale as indicated.

(E) Migration of MDA-MB-231 cells after transfection with either empty vector (CTL; gray) or ALDH1L2-overexpressing plasmid (OE-ALDH1L2; burgundy). Data are shown as mean ± SD of replicate wells pooled from 2 independent experiments. Unpaired t test, ****p < 0.0001.

(F) Migration of MDA-MB-468 cells after transfection with either non-targeting siRNA (siCTL; gray) or siALDH1L2 (orange) and treated with DMSO (CTL) or 50 μM MTP. Data are shown as mean ± SD of individual wells pooled from 2 independent experiments. Multiple comparison by one-way ANOVA, ***p < 0.001, ****p < 0.0001.

(G) Migration of MDA-MB-468 cells transfected with either non-targeting siRNA (siCTL; gray) or siALDH1L2 (orange) and treated with PBS (CTL) or 2 mM GSH. Data are shown as mean ± SD of triplicate or duplicate wells and represent 3 independent experiments. Multiple comparison by one-way ANOVA, **p < 0.01, ****p < 0.0001.

See also Figure S4.

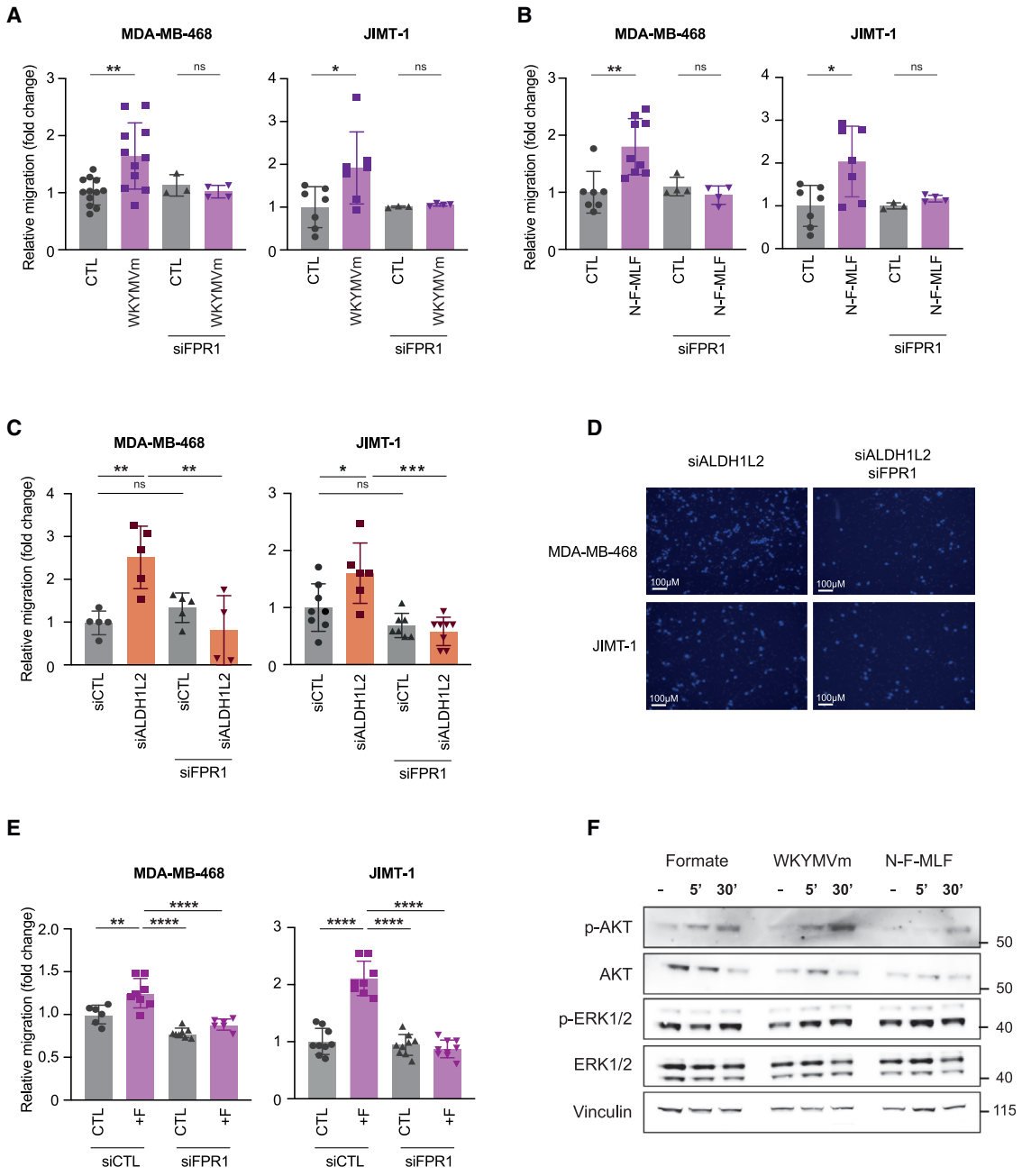

Figure 5. ALDH1L2 depletion promotes migration through FPR1

(A) Migration of MDA-MB-468 and JIMT-1 cells after transfection with siFPR1 and treatment with 20 μM WKYMVm, an FPR agonist (purple), or DMSO (CTL; gray). Data are shown as mean ± SD of individual wells pooled from 2 independent experiments. Multiple comparison by one-way ANOVA, *p < 0.05, **p < 0.01.

(B) Migration of MDA-MB-468 and JIMT-1 cells after transfection with siFPR1 and treatment with 50 μM N-F-Met-Leu-Phe (N-F-MLF) peptide, an FPR agonist (purple), or DMSO (CTL; gray). Data are shown as mean ± SD of individual wells pooled from 2 independent experiments. Unpaired t test, *p < 0.05, **p < 0.01.

(C) Migration of cells after transfection with either non-targeting siRNA (siCTL; gray), siALDH1L2 (orange), or siFPR1 (triangles). Data are shown as mean ± SD of individual wells pooled from 2 independent experiments. Multiple comparison by one-way ANOVA, *p < 0.05, **p < 0.01, ***p < 0.001.

(D) Representative images of DAPI-positive migrative cell quantified in (C). Scale as indicated.

(E) Migration of cells after treatment with PBS (CTL; gray) or 1 mM formate (purple) and transfection with either non-targeting siRNA (siCTL) or siFPR1. Data are shown as mean ± SD of individual wells pooled from 2 independent experiments. Multiple comparison by one-way ANOVA, **p < 0.01 , ****p < 0.0001.

(F) Western blot of AKT and ERK signaling after treatment of MDA-MB-231 cells with either 1 mM formate, 20 μM WKYMVm, or 50 μM N-F-MLF for 5 or 30 min. The same membrane was cut and probed for p-AKT and p-ERK1/2, then stripped and probed for total ERK and AKT.

See also Figure S5.

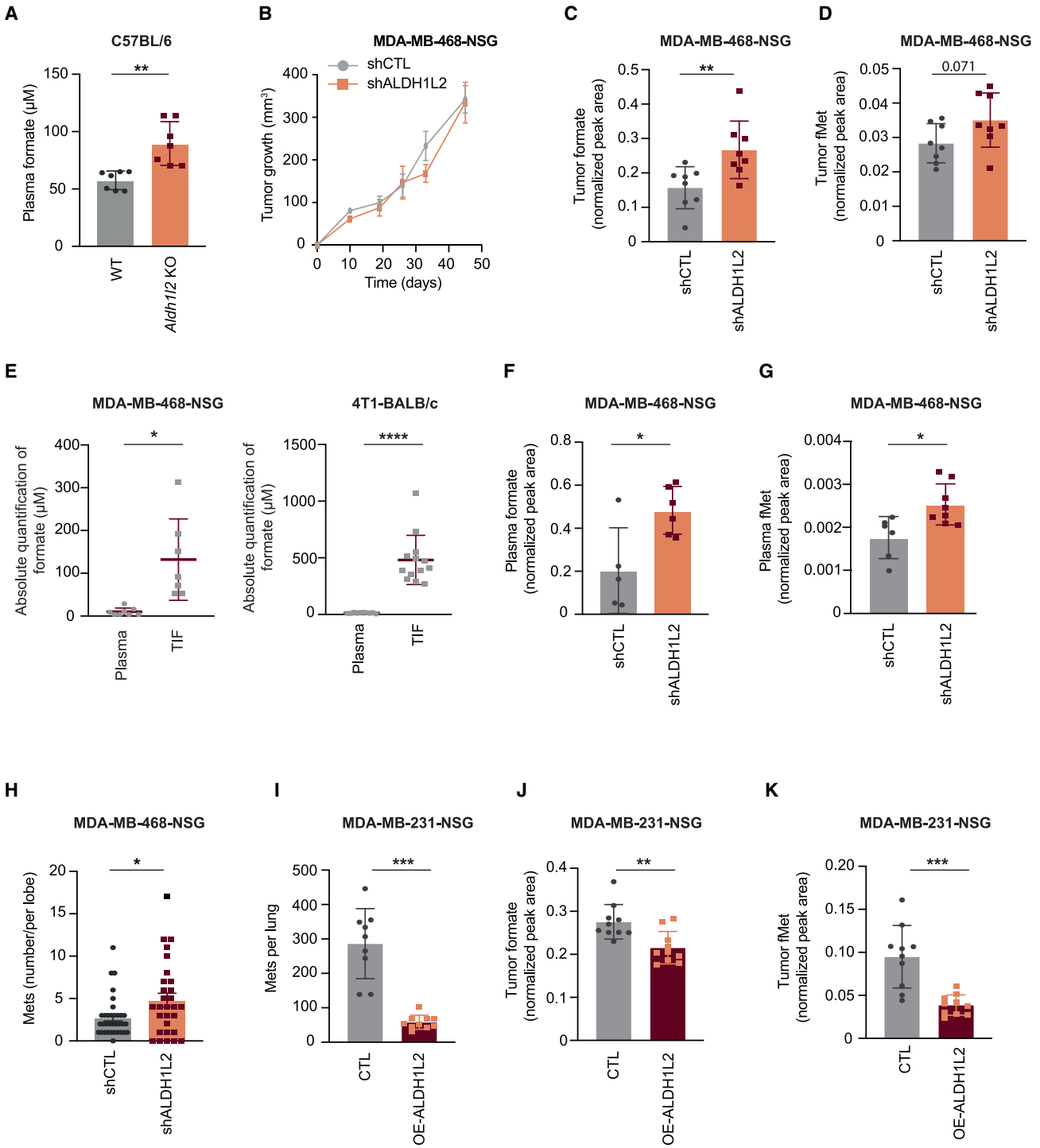

Figure 6. ALDH1L2 contribution to metastasis in immunodeficient mice

(A) Absolute quantification of formate by NMR in the plasma of C57BL/6 WT (gray; n = 7) or *Aldh1l2* KO mice (orange; n = 7). Data are shown as mean ± SD of individual animals, Unpaired t test, **p < 0.01.

(B) Tumor growth of WT MDA-MB-468 cells (gray; n = 8) or shALDH1L2 MDA-MB-468 cells (orange; n = 8) injected in the mammary fat pad of NOD.Cg-Prkdc^{scid} Il2rg^{tm1Wjl}/SzJ (NSG) mice. Data are shown as mean ± SD. Unpaired t test of tumor size at day 45.

(C) Levels of formate measured at time-matched endpoint by LC-MS in WT (shCTL; gray; n = 8) or ALDH1L2-depleted (shALDH1L2; orange; n = 8) MDA-MB-468 mammary fat pad tumors. Data are shown as mean ± SD. Unpaired t test, **p < 0.01.

(legend continued on next page)

was maintained throughout the experiment (Figure S6E). Both formate and fMet levels were increased in tumor tissue from these mice (Figures 6C and 6D), with increased formate levels and a trend (that was not significant) for increased fMet levels in the tumor interstitial fluid (TIF) (Figures S6F and S6G). Absolute quantification of formate in plasma and TIF revealed that levels of formate are, on average, 10- to 30-fold higher in TIF than in plasma of either MDA-MB-468 or 4T1 tumors (Figure 6E). We also detected increased formate and fMet levels in the plasma of mice bearing ALDH1L2-depleted MDA-MB-468 tumors (Figures 6F and 6G). While we found no significant difference in the number of mice with metastasis from MDA-MB-468 tumors, the metastatic burden per lung was significantly higher in mice carrying non-resected, ALDH1L2-depleted tumors (Figure 6H). Consistent with these results, increased circulating formate levels through dietary formate supplementation has been shown to enhance experimental metastasis of human colorectal cancer cells.[27] Similar analysis of MDA-MB-231 mammary fat pad tumors showed that ALDH1L2 overexpression led to a reduction in lung metastasis (Figure 6I), accompanied by decreased formate in tumor and TIF, and lower tumor fMet levels (Figures 6J, 6K, and S6H).

As formylated peptides play an important role in controlling immune cell function, we examined the role of ALDH1L2 on cancer development in immunocompetent models. To this end, we used 4T1 (BALB/c) and E0771 (C57BL/6) cells (neither of which express detectable levels of ALDH1L2) engineered to overexpress ALDH1L2. Expression of ALDH1L2 led to slightly increased proliferation of both cell lines *in vitro* (Figures S7A and S7B). *In vivo,* overexpression of ALDH1L2 in two independently derived 4T1 lines produced more rapidly growing tumors in the mammary fat pad of BALB/c mice (Figure 7A), although this was not accompanied by a significant increase in Ki67 staining (Figure S7C). Control and ALDH1L2-overexpressing E0771 mammary fat pad tumors grew at similar rates (Figure S7D). In both models, ALDH1L2-overexpressing tumors showed a decrease in tumor formate and fMet compared with control (Figures 7B, 7C, S7E, and S7F). These changes in formate and fMet levels were reflected in decreased infiltration of neutrophils (Figure 7D), a response that is associated with FPR activation and migration.[66] However, in the 4T1 model, there were no significant changes in the formate or fMet levels in the plasma or TIF in mice bearing ALDH1L2-overexpressing tumors (Figures S7G–S7J).

Expression of ALDH1L2 in 4T1 tumors did not result in a difference in the number of mice with metastases (Figures 7E and S7K) or the metastatic burden (Figures 7F and S7L). However, the E0771 model showed that ALDH1L2 overexpression resulted in trend toward less mice with metastases and a clear decrease in metastatic burden (Figures 7G and 7H). It seemed possible that the rapid growth of ALDH1L2-overexpressing 4T1 tumors may have complicated an assessment of metastatic capacity compared with control tumors. We therefore examined the behavior of these cells in an experimental model of metastasis, looking for lung colonization following tail vein injection. In this model, the ALDH1L2-overexpressing 4T1 cells showed a decrease in both number and extent of lung lesions (Figures 7I and 7J). Taken together, the results support a role for ALDH1L2 expression in limiting metastasis to the lung.

Turning back to the 4T1 mammary fat pad tumors, we noted a strong decrease in ALDH1L2 expression in the tumors cells compared with the starting overexpressing cell line (Figure S7M), with heterogeneous ALDH1L2 expression and Ki67 staining in the tumor tissue (Figures S7N and S7O). Importantly, the metastases that arose from the ALDH1L2-expressing tumors retained low or no ALDH1L2 expression (Figure 7K), consistent with an increased metastatic capacity of ALDH1L2-deficient cells. In the experimental metastasis model, where a reduction in lung colonization of the ALDH1L2-overexpressing 4T1 cells was seen, the lung colonies that were detected retained some ALDH1L2 expression (Figure 7L).

In human breast cancer, high expression of ALDH1L2 did not lead to differences in survival (Figure S7P), but an analysis of an expression database of primary breast tumors and matched brain metastasis[67,68] showed that ALDH1L2 expression is significantly lower in the metastasis than the primary tumor (Figure 7M). Available matched primary and metastatic expression data from TCGA database showed a similar result (Figure 7N), supporting the suggestion that loss of ALDH1L2 contributes to a higher rate of metastasis.

(D) Levels of fMet measured at time-matched endpoint by LC-MS in WT (shCTL; gray; n = 8) or ALDH1L2-depleted (shALDH1L2; orange; n = 8) MDA-MB-468 mammary fat pad tumors. Data are shown as mean ± SD. Unpaired t test.

(E) Absolute quantification of formate in the TIF and plasma by NMR. Left: NSG mice bearing MDA-MB-468 mammary fat pad tumors (plasma n = 8; TIF n = 7). Right: BALB/c mice bearing 4T1 mammary fat pad tumors (plasma n = 15; TIF n = 13). Unpaired Welch's t test,*p < 0.05, ****p < 0.001.

(F) Levels of formate measured at time-matched endpoint by LC-MS in the plasma of NSG mice bearing MDA-MB-468 WT (shCTL; gray; n = 5) or ALDH1L2-depleted (shALDH1L2; orange; n = 6) mammary fat pad tumors. Data are shown as mean ± SD. Unpaired t test, *p < 0.05.

(G) Levels of fMet measured at time-matched endpoint by LC-MS in the plasma of NSG mice bearing WT MDA-MB-468 cells (shCTL; gray; n = 6) or ALDH1L2-depleted (shALDH1L2; orange; n = 8) mammary fat pad tumors. Data are shown as mean ± SD of 6 individual mice per group. Unpaired t test, *p < 0.05.

(H) Number of metastases per lobe of tumor time-matched NSG mice bearing WT (shCTL; gray) or ALDH1L2-depleted (shALDH1L2; orange) MDA-MB-468 mammary fat pad tumors. The primary tumor was not resected. Data are shown as mean ± SD of individual lobes across 8 mice per group. Unpaired t test, *p < 0.05.

(I) Number of metastases per lung of tumor size-matched NSG mice bearing WT (CTL; gray; n = 9) or ALDH1L2-overexpressing (OE-ALDH1L2; burgundy; n = 10) MDA-MB-231 mammary fat pad tumors. The primary tumor was not resected. Data are shown as mean ± SD. Unpaired Welch's t test, ***p < 0.001.

(J) Levels of formate measured by LC-MS in WT (CTL; gray; n = 10) or ALDH1L2-overexpressing (OE-ALDH1L2; orange; n = 10) MDA-MB-231 mammary fat pad tumors. Data are shown as mean ± SD. Unpaired t test, **p < 0.01.

(K) Levels of fMet measured by LC-MS in WT (CTL; gray; n = 10) or ALDH1L2-overexpressing (OE-ALDH1L2; orange; n = 10) MDA-MB-231 mammary fat pad tumors. Data are shown as mean ± SD. Unpaired Welch's t test, ***p < 0.001.

See also Figure S6.

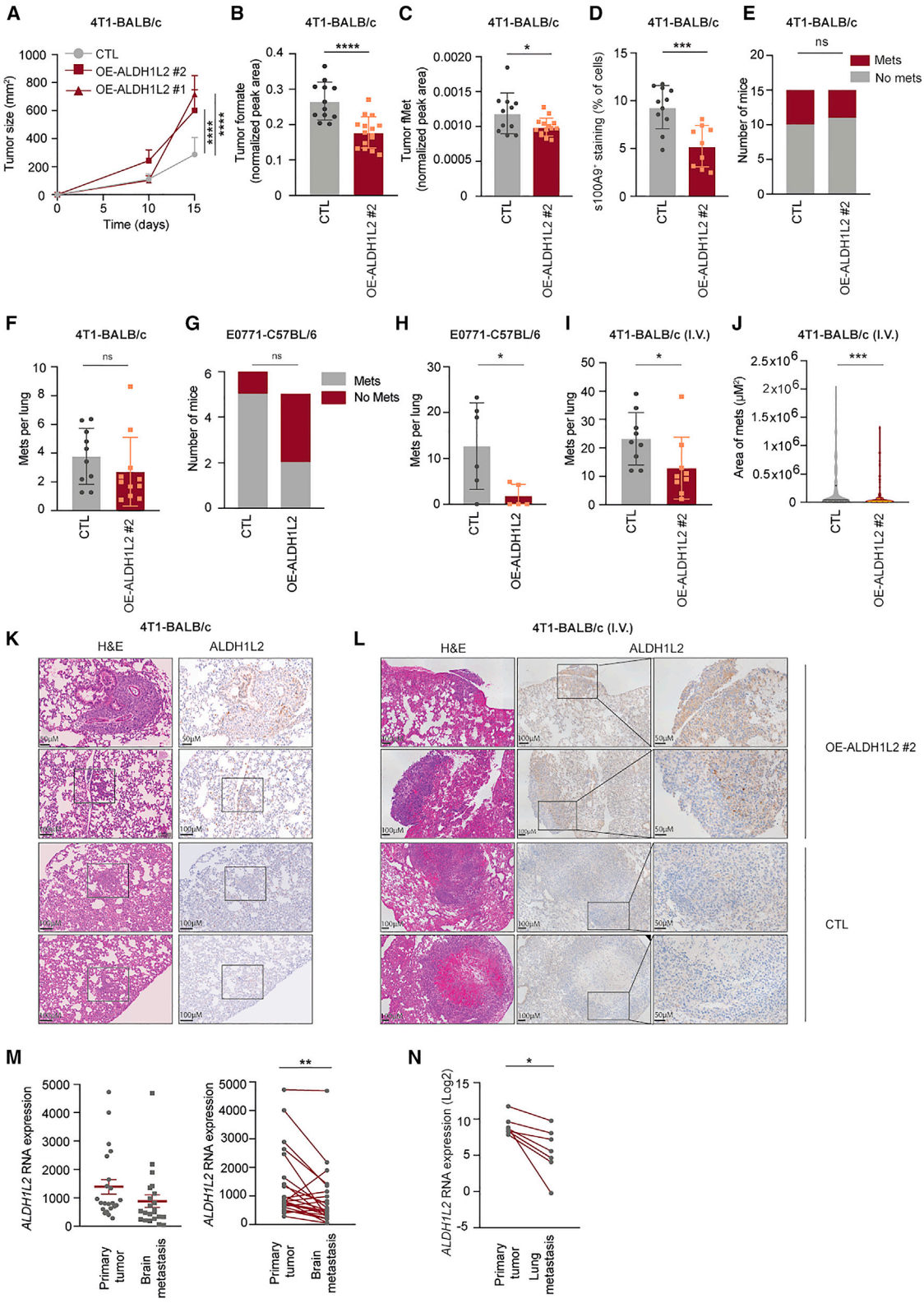

(legend on next page)

DISCUSSION

Human cancers show a wide range of ALDH1L2 expression levels, consistent with the observation that loss of ALDH1L2 can promote (as described here) or impede metastasis.[30] Such differential consequences of ALDH1L2 expression mirror the complexity of the role of ROS in driving cancer cell behavior, with evidence from numerous studies of both a pro- and antimetastatic response to increased ROS.[35] In our study, downregulation of ALDH1L2 expression promoted breast cancer cell migration, while serine starvation decreased migration. Intriguingly, both of these interventions lead to an increase in ROS (due to reduced NADPH and antioxidant capacity) but have opposing effects on formate and fMet production (serine starvation reducing and ALDH1L2 loss increasing formate and fMet levels). These results therefore indicate that in this system, the increased migration results principally from increased formate and fMet levels. We find that both formate and fMet induce migration through FPR-dependent signaling, with evidence that excess formate leads to increased fMet levels. While other functions of formate—such as an ability to support mitochondrial translation through tRNA methylation[69]—may also contribute to this response, our data provide a clear pathway through which increased formate and fMet levels can provoke signaling through pathways such as AKT, which are well-established mediators of cell migration and cancer metastasis. Interestingly, while SSP activity has been linked to increased invasion and metastasis,[24,25] high expression of PHGDH—the first enzyme in the SSP—has recently been shown to decrease metastatic disease through a direct interaction of PHGDH with phosphofructokinase and consequent alterations in protein glycosylation.[70] In this context, it is worth noting that serine starvation leads to increased PHGDH expression,[71,72] highlighting the complexity of the mechanisms through which serine metabolism affects tumor progression.

While we have focused on the consequences of formate and fMet production on the behavior of the cancer cells themselves, their production by tumors could also have profound effects on the tumor microenvironment. Although formate supplementation in the diet was not found to influence general levels of circulating or splenic lymphocyte,[73] *in vitro* studies have shown that supplementation of one-carbon units in the form of glycine and formate rescue T cell activation in aging mice.[74,75] This is consistent with the importance of both the cytosolic and mitochondrial one-carbon metabolism in T cell activation both in mice and humans.[76,77] In addition to formate, formylated peptides are well-established chemo-attractants of innate immune cells that can have secondary effects on the adaptive immune system. For example, FPR1-expressing immune cells such as dendritic cells or neutrophils (which we showed to be modulated by ALDH1L2 expression in the tumor) are attracted by the release of formylated peptides from dying cancer cells.[78] Therefore, modulation of formate and fMet levels by ALDH1L2 in tumors could affect not only tumor cell migration but also the infiltration and activation of immune cells. Finally, ROS in the tumor microenvironment is also known to inhibit T cell activation and favor an immunosuppressive environment.[79,80] The prediction of the outcome of ALDH1L2 depletion is therefore complex, balancing alterations in cancer cell migration with enhanced immune cell attraction and modulation. We note a recent study showing that formate in the drinking water not only favored Th17 T cell expansion in the mesenteric lymph nodes of colorectal cancer bearing mice

Figure 7. ALDH1L2 contribution to tumor growth and metastasis in immunocompetent mice

(A) Tumor growth of WT 4T1 cells (CTL; gray; n = 27) or ALDH1L2-overexpressing 4T1 cells (OE-ALDH1L2 #1, n = 15 and OE-ALDH1L2 #2, n = 11; burgundy) injected in the mammary fat pad of BALB/c mice. Data are shown as mean ± SD. Multiple comparison by one-way ANOVA of tumor size at day 15, ****$p < 0.0001$.

(B) Levels of formate measured at time-matched endpoint by LC-MS in WT 4T1 (CTL; gray) or ALDH1L2-overexpressing 4T1 (OE-ALDH1L2 #2; burgundy) mammary fat pad tumors. Data are shown as mean ± SD of CTL (n = 12) and OE-ALDH1L2 (n = 15) mice. Unpaired t test, ****$p < 0.0001$.

(C) Levels of fMet measured at time-matched endpoint by LC-MS in WT 4T1 (CTL; gray) or ALDH1L2-overexpressing 4T1 (OE-ALDH1L2 #2; burgundy) mammary fat pad tumors. Data are shown as mean ± SD of CTL (n = 11) and OE-ALDH1L2 #2 (n = 14) mice. Unpaired t test, *$p < 0.05$.

(D) Percentage of $S100A9^+$ cells in WT 4T1 l (CTL; gray; n = 10) or ALDH1L2-overexpressing 4T1 (OE-ALDH1L2 #2; burgundy; n = 10) mammary fat pad tumors as measured by immunohistochemistry. Data are shown as mean ± SD. Unpaired t test, ***$p < 0.001$.

(E) Number of 4T1 WT (n = 15) or OE-ALDH1L2 #2 time-matched (n = 15) tumor-bearing BALB/c mice harboring metastatic lesions in the lung. The primary tumor was not resected. Fisher's exact test.

(F) Number of metastases per lung normalized by tumor volume in BALB/c mice bearing 4T1 WT (CTL; gray; n = 10) or ALDH1L2-overexpressing (OE-ALDH1L2 #2; burgundy; n = 11) time-matched mammary fat pad tumors. The primary tumor was not resected. Data are shown as mean ± SD. Unpaired t test.

(G) Number of E0771 WT (n = 6) or OE-ALDH1L2 time-matched (n = 5) tumor-bearing C57BL/6 mice harboring metastatic lesions in the lung. The primary tumor was not resected. Fisher's exact test.

(H) Number of metastases per lung normalized by tumor volume of C57BL/6 mice bearing E0771 WT (CTL; gray; n = 6) or ALDH1L2-overexpressing (OE-ALDH1L2; burgundy; n = 5) time-matched mammary fat pad tumors. The primary tumor was not resected. Data are shown as mean ± SD. Unpaired t test, *$p < 0.05$.

(I) Number of metastases per lung of BALB/c mice intravenously injected with 4T1 WT (CTL; gray; n = 9) or ALDH1L2-overexpressing (OE-ALDH1L2; burgundy; n = 9) cells. Data are shown as mean ± SD. Unpaired t test, *$p < 0.05$.

(J) Area of metastasis observed in (I). Unpaired t test, ***$p < 0.001$.

(K) Representative H&E and ALDH1L2 staining of metastatic lesions in the lungs of ALDH1L2-overexpressing 4T1 mammary fat pad tumors quantified in (F). Scale as indicated.

(L) Representative H&E and ALDH1L2 staining of metastatic lesions in the lungs of BALB/c mice intravenously injected with WT (CTL) or ALDH1L2-overexpressing (OE-ALDH1L2) 4T1 cells quantified in (I). Scale as indicated.

(M) *ALDH1L2* RNA expression in human primary breast tumors and matching brain metastasis. Left panel: data are shown as mean ± SD of 22 patients for primary and metastasis tissue. Right panel: data are shown as matched pairs. Paired t test, **$p < 0.001$.

(N) *ALDH1L2* RNA expression extracted from TCGA database of primary tumors and matched metastasis. Paired t test, *$p < 0.05$.

See also Figure S7.

but also increased cancer formation through increased stemness,[27] highlighting the potentially opposing responses to increased formate production on tumorigenesis.

Circulating formate levels can be influenced by several factors, including diet and bacteria of the gut microbiota.[27] We showed an increase in circulating formate in mice bearing ALDH1L2-depleted tumors, correlating with enhanced metastasis. Interestingly, increased formate production is also seen in response to other oncogenic alterations such as the K-RAS mutation.[81] It is possible that circulating formate could serve as a biomarker for cancers with high formate overflow and increased metastatic potential.

Limitations of the study

We have not identified the source of fMet in our studies, which could be derived from fMet-tRNA or the cleavage of f-Met-containing proteins. However, FPRs require peptides of at least 3 amino acids to be efficiently activated,[82] and we find that fMet itself has no effect on the migration, suggesting that this response is mediated through protein-derived formylated peptides.[83] While treatment of cells with formate also promoted FPR-dependent migration, our work does not preclude other functions of formate in mediating this response.

Use of metastasis models in which the primary tumor is resected would allow a more detailed analysis of the metastatic process and more closely mimic the situation in patients.

We have not fully assessed the effect of ALDH1L2 modulation of fMet and formate production on the immune response to cancer development or determined whether ALDH1L2-driven changes in pro- or antitumor immune responses impact the metastatic phenotypes described in this study. Our work in immunocompetent mice is limited to the use of cells ectopically overexpressing ALDH1L2. Examination of the effects of modulating endogenous ALDH1L2 in genetically engineered mouse models of cancer would be more physiologically relevant.

STAR★METHODS

Detailed methods are provided in the online version of this paper and include the following:

SUPPLEMENTAL INFORMATION

Supplemental information can be found online at https://doi.org/10.1016/j.celrep.2023.112562.

ACKNOWLEDGMENTS

The authors would like to thank the following: Prof. Joshua Rabinowitz for sharing his liquid chromatography-mass spectrometry (LC-MS) derivatization protocol for formate detection, Prof. Stamp for evaluating the histopathology of mouse models, the Crick BRF for helping with the animal experiments, and the Crick flow cytometry facility for helping with sorting and flow cytometry experiments. Metabolomic analysis was supported by Dr. James Macrae and the metabolomics STP of the Francis Crick Institute and through provision of access to the MRC Biomedical NMR Centre. The work was funded by Cancer Research UK grant C596/A26855 and supported by the Francis Crick Institute, which receives its core funding from Cancer Research UK (CC2073), the UK Medical Research Council (CC2073), and the Wellcome Trust (CC2073). J.B. is funded by the Kuok Family Fellowship. C.S. is a Royal Society Napier Research Professor (RSRP\R\210001). His work is supported by the Francis Crick Institute, which receives its core funding from Cancer Research UK (CC2041), the UK Medical Research Council (CC2041), and the Wellcome Trust (CC2041). C.S. and E.G. are supported by an ERC Advanced Grant (PROTEUS, grant agreement no. 835297). M.Y. is supported by the Francis Crick Institute, which receives its core funding from Cancer Research UK (CC2082), the UK Medical Research Council (CC2082), and the Wellcome Trust (CC2082). For the purpose of open access, the author has applied a CC BY public copyright license to any author-accepted manuscript version arising from this submission.

AUTHOR CONTRIBUTIONS

M.H., C.F.L., and K.H.V. conceptualized the study. M.H. performed and designed most experiments and analyzed the data. S.E.P. and Y.L. performed *in vitro* overexpression experiments and were involved in the experimental design. S.E.P., P.K., L.M., and E.C.C. performed animal experiments and were involved in experimental design. E.G. provided advice and guidance on metastatic models. B.M. and Y.P. performed and analyzed MMTV-MYC experiments. D. Stevenson and D. Strathdee generated the ALDH1L2 KO mouse. J.C. performed immunohistochemistry optimization, staining, and analysis. N.M.L. and M.H. optimized LC-MS formate detection and ran LC-MS experiments. P.C.D. performed and analyzed NMR detection of formate. J.B. and C.S. provided scientific advice. D.S.-L. performed *in silico* analysis. M.Y. provided MMTV-MYC model, data, and scientific advice. M.H. and K.H.V. wrote the manuscript.

DECLARATION OF INTERESTS

K.H.V. is on the board of directors and is a shareholder of Bristol Myers Squibb and is on the scientific advisory board (with stock options) of PMV Pharma, RAZE Therapeutics, Volastra Pharmaceuticals, and Kovina Therapeutics. She is on the scientific advisory board (SAB) of Ludwig Cancer and is a co-founder and consultant of Faeth Therapeutics. She has been in receipt of research funding from Astex Pharmaceuticals and AstraZeneca and

contributed to the CRUK Cancer Research Technology filing of patent application WO/2017/144877. C.S. acknowledges grant support from AstraZeneca, Boehringer-Ingelheim, Bristol Myers Squibb, Pfizer, Roche-Ventana, Invitae (previously Archer Dx, Inc., collaboration in minimal residual disease sequencing technologies), Ono Pharmaceutical, and Personalis. He is an AstraZeneca advisory board member, chief investigator for the AZ MeRmaiD 1 and 2 clinical trials, co-chief investigator of the NHS Galleri trial funded by GRAIL, and a paid member of GRAIL's SAB. He receives consultant fees from Achilles Therapeutics (also a SAB member), Bicycle Therapeutics (also a SAB member), Genentech, Medicxi, China Innovation Center of Roche (CICoR), formerly the Roche Innovation Center – Shanghai, Metabomed (until July 2022), and the Sarah Cannon Research Institute. C.S. has received honoraria from Amgen, AstraZeneca, Pfizer, Novartis, GlaxoSmithKline, MSD, Bristol Myers Squibb, Illumina, and Roche-Ventana. C.S. had stock options in Apogen Biotechnologies and GRAIL until June 2021 and currently has stock options in Epic Bioscience and Bicycle Therapeutics and has stock options and is co-founder of Achilles Therapeutics.

Received: August 10, 2022
Revised: March 10, 2023
Accepted: May 9, 2023

REFERENCES

1. Tibbetts, A.S., and Appling, D.R. (2010). Compartmentalization of Mammalian folate-mediated one-carbon metabolism. Annu. Rev. Nutr. *30*, 57–81. https://doi.org/10.1146/annurev.nutr.012809.104810.
2. Yang, M., and Vousden, K.H. (2016). Serine and one-carbon metabolism in cancer. Nat. Rev. Cancer *16*, 650–662. https://doi.org/10.1038/nrc.2016.81.
3. Locasale, J.W. (2013). Serine, glycine and one-carbon units: cancer metabolism in full circle. Nat. Rev. Cancer *13*, 572–583. https://doi.org/10.1038/nrc3557.
4. Gonen, N., and Assaraf, Y.G. (2012). Antifolates in cancer therapy: structure, activity and mechanisms of drug resistance. Drug Resist. Updates *15*, 183–210. https://doi.org/10.1016/j.drup.2012.07.002.
5. Nilsson, R., Jain, M., Madhusudhan, N., Sheppard, N.G., Strittmatter, L., Kampf, C., Huang, J., Asplund, A., and Mootha, V.K. (2014). Metabolic enzyme expression highlights a key role for MTHFD2 and the mitochondrial folate pathway in cancer. Nat. Commun. *5*, 3128. https://doi.org/10.1038/ncomms4128.
6. Ye, J., Fan, J., Venneti, S., Wan, Y.W., Pawel, B.R., Zhang, J., Finley, L.W.S., Lu, C., Lindsten, T., Cross, J.R., et al. (2014). Serine catabolism regulates mitochondrial redox control during hypoxia. Cancer Discov. *4*, 1406–1417. https://doi.org/10.1158/2159-8290.CD-14-0250.
7. Li, A.M., Ducker, G.S., Li, Y., Seoane, J.A., Xiao, Y., Melemenidis, S., Zhou, Y., Liu, L., Vanharanta, S., Graves, E.E., et al. (2020). Metabolic profiling reveals a dependency of human metastatic breast cancer on mitochondrial serine and one-carbon unit metabolism. Mol. Cancer Res. *18*, 599–611. https://doi.org/10.1158/1541-7786.MCR-19-0606.
8. Bernhardt, S., Bayerlová, M., Vetter, M., Wachter, A., Mitra, D., Hanf, V., Lantzsch, T., Uleer, C., Peschel, S., John, J., et al. (2017). Proteomic profiling of breast cancer metabolism identifies SHMT2 and ASCT2 as prognostic factors. Breast Cancer Res. *19*, 112. https://doi.org/10.1186/s13058-017-0905-7.
9. Lehtinen, L., Ketola, K., Mäkelä, R., Mpindi, J.P., Viitala, M., Kallioniemi, O., and Iljin, K. (2013). High-throughput RNAi screening for novel modulators of vimentin expression identifies MTHFD2 as a regulator of breast cancer cell migration and invasion. Oncotarget *4*, 48–63. https://doi.org/10.18632/oncotarget.756.
10. Mullarky, E., Lucki, N.C., Beheshti Zavareh, R., Anglin, J.L., Gomes, A.P., Nicolay, B.N., Wong, J.C.Y., Christen, S., Takahashi, H., Singh, P.K., et al. (2016). Identification of a small molecule inhibitor of 3-phosphoglycerate dehydrogenase to target serine biosynthesis in cancers. Proc. Natl. Acad. Sci. USA *113*, 1778–1783. https://doi.org/10.1073/pnas.1521548113.
11. Possemato, R., Marks, K.M., Shaul, Y.D., Pacold, M.E., Kim, D., Birsoy, K., Sethumadhavan, S., Woo, H.K., Jang, H.G., Jha, A.K., et al. (2011). Functional genomics reveal that the serine synthesis pathway is essential in breast cancer. Nature *476*, 346–350. https://doi.org/10.1038/nature10350.
12. Pacold, M.E., Brimacombe, K.R., Chan, S.H., Rohde, J.M., Lewis, C.A., Swier, L.J.Y.M., Possemato, R., Chen, W.W., Sullivan, L.B., Fiske, B.P., et al. (2016). A PHGDH inhibitor reveals coordination of serine synthesis and one-carbon unit fate. Nat. Chem. Biol. *12*, 452–458. https://doi.org/10.1038/nchembio.2070.
13. Locasale, J.W., Grassian, A.R., Melman, T., Lyssiotis, C.A., Mattaini, K.R., Bass, A.J., Heffron, G., Metallo, C.M., Muranen, T., Sharfi, H., et al. (2011). Phosphoglycerate dehydrogenase diverts glycolytic flux and contributes to oncogenesis. Nat. Genet. *43*, 869–874. https://doi.org/10.1038/ng.890.
14. Sullivan, M.R., Mattaini, K.R., Dennstedt, E.A., Nguyen, A.A., Sivanand, S., Reilly, M.F., Meeth, K., Muir, A., Darnell, A.M., Bosenberg, M.W., et al. (2019). Increased serine synthesis provides an advantage for tumors arising in tissues where serine levels are limiting. Cell Metabol. *29*, 1410–1421.e4. https://doi.org/10.1016/j.cmet.2019.02.015.
15. Maddocks, O.D.K., Athineos, D., Cheung, E.C., Lee, P., Zhang, T., van den Broek, N.J.F., Mackay, G.M., Labuschagne, C.F., Gay, D., Kruiswijk, F., et al. (2017). Modulating the therapeutic response of tumours to dietary serine and glycine starvation. Nature *544*, 372–376. https://doi.org/10.1038/nature22056.
16. Tajan, M., Hennequart, M., Cheung, E.C., Zani, F., Hock, A.K., Legrave, N., Maddocks, O.D.K., Ridgway, R.A., Athineos, D., Suárez-Bonnet, A., et al. (2021). Serine synthesis pathway inhibition cooperates with dietary serine and glycine limitation for cancer therapy. Nat. Commun. *12*, 366. https://doi.org/10.1038/s41467-020-20223-y.
17. Tait-Mulder, J., Hodge, K., Sumpton, D., Zanivan, S., and Vazquez, A. (2020). The conversion of formate into purines stimulates mTORC1 leading to CAD-dependent activation of pyrimidine synthesis. Cancer Metabol. *8*, 20. https://doi.org/10.1186/s40170-020-00228-3.
18. Oizel, K., Tait-Mulder, J., Fernandez-de-Cossio-Diaz, J., Pietzke, M., Brunton, H., Lilla, S., Dhayade, S., Athineos, D., Blanco, G.R., Sumpton, D., et al. (2020). Formate induces a metabolic switch in nucleotide and energy metabolism. Cell Death Dis. *11*, 310. https://doi.org/10.1038/s41419-020-2523-z.
19. Meiser, J., Tumanov, S., Maddocks, O., Labuschagne, C.F., Athineos, D., Van Den Broek, N., Mackay, G.M., Gottlieb, E., Blyth, K., Vousden, K., et al. (2016). Serine one-carbon catabolism with formate overflow. Sci. Adv. *2*, e1601273. https://doi.org/10.1126/sciadv.1601273.
20. Balsa, E., Perry, E.A., Bennett, C.F., Jedrychowski, M., Gygi, S.P., Doench, J.G., and Puigserver, P. (2020). Defective NADPH production in mitochondrial disease complex I causes inflammation and cell death. Nat. Commun. *11*, 2714. https://doi.org/10.1038/s41467-020-16423-1.
21. Fan, J., Ye, J., Kamphorst, J.J., Shlomi, T., Thompson, C.B., and Rabinowitz, J.D. (2014). Quantitative flux analysis reveals folate-dependent NADPH production. Nature *510*, 298–302. https://doi.org/10.1038/nature13236.
22. Minton, D.R., Nam, M., McLaughlin, D.J., Shin, J., Bayraktar, E.C., Alvarez, S.W., Sviderskiy, V.O., Papagiannakopoulos, T., Sabatini, D.M., Birsoy, K., and Possemato, R. (2018). Serine catabolism by SHMT2 is required for proper mitochondrial translation initiation and maintenance of formylmethionyl-tRNAs. Mol. Cell *69*, 610–621.e5. https://doi.org/10.1016/j.molcel.2018.01.024.
23. Tucker, E.J., Hershman, S.G., Köhrer, C., Belcher-Timme, C.A., Patel, J., Goldberger, O.A., Christodoulou, J., Silberstein, J.M., McKenzie, M., Ryan, M.T., et al. (2011). Mutations in MTFMT underlie a human disorder of formylation causing impaired mitochondrial translation. Cell Metabol. *14*, 428–434. https://doi.org/10.1016/j.cmet.2011.07.010.

24. Soflaee, M.H., Kesavan, R., Sahu, U., Tasdogan, A., Villa, E., Djabari, Z., Cai, F., Tran, D.H., Vu, H.S., Ali, E.S., et al. (2022). Purine nucleotide depletion prompts cell migration by stimulating the serine synthesis pathway. Nat. Commun. *13*, 2698. https://doi.org/10.1038/s41467-022-30362-z.

25. Kiweler, N., Delbrouck, C., Pozdeev, V.I., Neises, L., Soriano-Baguet, L., Eiden, K., Xian, F., Benzarti, M., Haase, L., Koncina, E., et al. (2022). Mitochondria preserve an autarkic one-carbon cycle to confer growth-independent cancer cell migration and metastasis. Nat. Commun. *13*, 2699. https://doi.org/10.1038/s41467-022-30363-y.

26. Meiser, J., Schuster, A., Pietzke, M., Vande Voorde, J., Athineos, D., Oizel, K., Burgos-Barragan, G., Wit, N., Dhayade, S., Morton, J.P., et al. (2018). Increased formate overflow is a hallmark of oxidative cancer. Nat. Commun. *9*, 1368. https://doi.org/10.1038/s41467-018-03777-w.

27. Ternes, D., Tsenkova, M., Pozdeev, V.I., Meyers, M., Koncina, E., Atatri, S., Schmitz, M., Karta, J., Schmoetten, M., Heinken, A., et al. (2022). The gut microbial metabolite formate exacerbates colorectal cancer progression. Nat. Metab. *4*, 458–475. https://doi.org/10.1038/s42255-022-00558-0.

28. Newman, A.C., and Maddocks, O.D.K. (2017). Serine and functional metabolites in cancer. Trends Cell Biol. *27*, 645–657. https://doi.org/10.1016/j.tcb.2017.05.001.

29. Zhang, Z., TeSlaa, T., Xu, X., Zeng, X., Yang, L., Xing, G., Tesz, G.J., Clasquin, M.F., and Rabinowitz, J.D. (2021). Serine catabolism generates liver NADPH and supports hepatic lipogenesis. Nat. Metab. *3*, 1608–1620. https://doi.org/10.1038/s42255-021-00487-4.

30. Piskounova, E., Agathocleous, M., Murphy, M.M., Hu, Z., Huddlestun, S.E., Zhao, Z., Leitch, A.M., Johnson, T.M., DeBerardinis, R.J., and Morrison, S.J. (2015). Oxidative stress inhibits distant metastasis by human melanoma cells. Nature *527*, 186–191. https://doi.org/10.1038/nature15726.

31. Porporato, P.E., Payen, V.L., Pérez-Escuredo, J., De Saedeleer, C.J., Danhier, P., Copetti, T., Dhup, S., Tardy, M., Vazeille, T., Bouzin, C., et al. (2014). A mitochondrial switch promotes tumor metastasis. Cell Rep. *8*, 754–766. https://doi.org/10.1016/j.celrep.2014.06.043.

32. Le Gal, K., Ibrahim, M.X., Wiel, C., Sayin, V.I., Akula, M.K., Karlsson, C., Dalin, M.G., Akyürek, L.M., Lindahl, P., Nilsson, J., and Bergo, M.O. (2015). Antioxidants can increase melanoma metastasis in mice. Sci. Transl. Med. *7*, 308re8. https://doi.org/10.1126/scitranslmed.aad3740.

33. Cheung, E.C., DeNicola, G.M., Nixon, C., Blyth, K., Labuschagne, C.F., Tuveson, D.A., and Vousden, K.H. (2020). Dynamic ROS control by TIGAR regulates the initiation and progression of pancreatic cancer. Cancer Cell *37*, 168–182.e4. https://doi.org/10.1016/j.ccell.2019.12.012.

34. Arnandis, T., Monteiro, P., Adams, S.D., Bridgeman, V.L., Rajeeve, V., Gadaleta, E., Marzec, J., Chelala, C., Malanchi, I., Cutillas, P.R., and Godinho, S.A. (2018). Oxidative stress in cells with extra centrosomes drives non-cell-autonomous invasion. Dev. Cell *47*, 409–424.e9. https://doi.org/10.1016/j.devcel.2018.10.026.

35. Cheung, E.C., and Vousden, K.H. (2022). The role of ROS in tumour development and progression. Nat. Rev. Cancer *22*, 280–297. https://doi.org/10.1038/s41568-021-00435-0.

36. Koseki, J., Konno, M., Asai, A., Colvin, H., Kawamoto, K., Nishida, N., Sakai, D., Kudo, T., Satoh, T., Doki, Y., et al. (2018). Enzymes of the one-carbon folate metabolism as anticancer targets predicted by survival rate analysis. Sci. Rep. *8*, 303. https://doi.org/10.1038/s41598-017-18456-x.

37. Miyo, M., Konno, M., Colvin, H., Nishida, N., Koseki, J., Kawamoto, K., Tsunekuni, K., Nishimura, J., Hata, T., Takemasa, I., et al. (2017). The importance of mitochondrial folate enzymes in human colorectal cancer. Oncol. Rep. *37*, 417–425. https://doi.org/10.3892/or.2016.5264.

38. Chang, P.M.H., Chen, C.H., Yeh, C.C., Lu, H.J., Liu, T.T., Chen, M.H., Liu, C.Y., Wu, A.T.H., Yang, M.H., Tai, S.K., et al. (2018). Transcriptome analysis and prognosis of ALDH isoforms in human cancer. Sci. Rep. *8*, 2713. https://doi.org/10.1038/s41598-018-21123-4.

39. Vasan, K., Werner, M., and Chandel, N.S. (2020). Mitochondrial metabolism as a target for cancer therapy. Cell Metabol. *32*, 341–352. https://doi.org/10.1016/j.cmet.2020.06.019.

40. Maddocks, O.D.K., Berkers, C.R., Mason, S.M., Zheng, L., Blyth, K., Gottlieb, E., and Vousden, K.H. (2013). Serine starvation induces stress and p53-dependent metabolic remodelling in cancer cells. Nature *493*, 542–546. https://doi.org/10.1038/nature11743.

41. Aslakson, C.J., and Miller, F.R. (1992). Selective events in the metastatic process defined by analysis of the sequential dissemination of subpopulations of a mouse mammary tumor. Cancer Res. *52*, 1399–1405.

42. Yang, S., Zhang, J.J., and Huang, X.Y. (2012). Mouse models for tumor metastasis. Methods Mol. Biol. *928*, 221–228. https://doi.org/10.1007/978-1-62703-008-3_17.

43. Zhang, Y., Zhang, G.L., Sun, X., Cao, K.X., Ma, C., Nan, N., Yang, G.W., Yu, M.W., and Wang, X.M. (2018). Establishment of a murine breast tumor model by subcutaneous or orthotopic implantation. Oncol. Lett. *15*, 6233–6240. https://doi.org/10.3892/ol.2018.8113.

44. Taneja, P., Frazier, D.P., Kendig, R.D., Maglic, D., Sugiyama, T., Kai, F., Taneja, N.K., and Inoue, K. (2009). MMTV mouse models and the diagnostic values of MMTV-like sequences in human breast cancer. Expert Rev. Mol. Diagn. *9*, 423–440. https://doi.org/10.1586/erm.09.31.

45. Stewart, T.A., Pattengale, P.K., and Leder, P. (1984). Spontaneous mammary adenocarcinomas in transgenic mice that carry and express MTV/myc fusion genes. Cell *38*, 627–637. https://doi.org/10.1016/0092-8674(84)90257-5.

46. Ducker, G.S., Chen, L., Morscher, R.J., Ghergurovich, J.M., Esposito, M., Teng, X., Kang, Y., and Rabinowitz, J.D. (2016). Reversal of cytosolic one-carbon flux compensates for loss of the mitochondrial folate pathway. Cell Metabol. *23*, 1140–1153. https://doi.org/10.1016/j.cmet.2016.04.016.

47. Krupenko, N.I., Dubard, M.E., Strickland, K.C., Moxley, K.M., Oleinik, N.V., and Krupenko, S.A. (2010). ALDH1L2 is the mitochondrial homolog of 10-formyltetrahydrofolate dehydrogenase. J. Biol. Chem. *285*, 23056–23063. https://doi.org/10.1074/jbc.M110.128843.

48. Krupenko, N.I., Sharma, J., Pediaditakis, P., Helke, K.L., Hall, M.S., Du, X., Sumner, S., and Krupenko, S.A. (2020). Aldh1l2 knockout mouse metabolomics links the loss of the mitochondrial folate enzyme to deregulation of a lipid metabolism observed in rare human disorder. Hum. Genom. *14*, 41. https://doi.org/10.1186/s40246-020-00291-3.

49. Cheung, E.C., Athineos, D., Lee, P., Ridgway, R.A., Lambie, W., Nixon, C., Strathdee, D., Blyth, K., Sansom, O.J., and Vousden, K.H. (2013). TIGAR is required for efficient intestinal regeneration and tumorigenesis. Dev. Cell *25*, 463–477. https://doi.org/10.1016/j.devcel.2013.05.001.

50. Lewis, C.A., Parker, S.J., Fiske, B.P., McCloskey, D., Gui, D.Y., Green, C.R., Vokes, N.I., Feist, A.M., Vander Heiden, M.G., and Metallo, C.M. (2014). Tracing compartmentalized NADPH metabolism in the cytosol and mitochondria of mammalian cells. Mol. Cell *55*, 253–263. https://doi.org/10.1016/j.molcel.2014.05.008.

51. Schiffmann, E., Corcoran, B.A., and Wahl, S.M. (1975). N-formylmethionyl peptides as chemoattractants for leucocytes. Proc. Natl. Acad. Sci. USA *72*, 1059–1062. https://doi.org/10.1073/pnas.72.3.1059.

52. Wenceslau, C.F., Szasz, T., McCarthy, C.G., Baban, B., NeSmith, E., and Webb, R.C. (2016). Mitochondrial N-formyl peptides cause airway contraction and lung neutrophil infiltration via formyl peptide receptor activation. Pulm. Pharmacol. Ther. *37*, 49–56. https://doi.org/10.1016/j.pupt.2016.02.005.

53. Shao, G., Julian, M.W., Bao, S., McCullers, M.K., Lai, J.P., Knoell, D.L., and Crouser, E.D. (2011). Formyl peptide receptor ligands promote wound closure in lung epithelial cells. Am. J. Respir. Cell Mol. Biol. *44*, 264–269. https://doi.org/10.1165/rcmb.2010-0246RC.

54. Itagaki, K., Kaczmarek, E., Kwon, W.Y., Chen, L., Vlková, B., Zhang, Q., Riça, I., Yaffe, M.B., Campbell, Y., Marusich, M.F., et al. (2020). Formyl peptide receptor-1 blockade prevents receptor regulation by mitochondrial danger-associated molecular patterns and preserves neutrophil

function after trauma. Crit. Care Med. *48*, e123–e132. https://doi.org/10.1097/CCM.0000000000004094.

55. Wickstead, E.S., Solito, E., and McArthur, S. (2022). Promiscuous receptors and neuroinflammation: the formyl peptide class. Life *12*, 2009. https://doi.org/10.3390/life12122009.

56. Li, S.Q., Su, N., Gong, P., Zhang, H.B., Liu, J., Wang, D., Sun, Y.P., Zhang, Y., Qian, F., Zhao, B., et al. (2017). The expression of formyl peptide receptor 1 is correlated with tumor invasion of human colorectal cancer. Sci. Rep. *7*, 5918. https://doi.org/10.1038/s41598-017-06368-9.

57. Ahmet, D.S., Basheer, H.A., Salem, A., Lu, D., Aghamohammadi, A., Weyerhäuser, P., Bordiga, A., Almeniawi, J., Rashid, S., Cooper, P.A., et al. (2020). Application of small molecule FPR1 antagonists in the treatment of cancers. Sci. Rep. *10*, 17249. https://doi.org/10.1038/s41598-020-74350-z.

58. Shaul, Y.D., Yuan, B., Thiru, P., Nutter-Upham, A., McCallum, S., Lanzkron, C., Bell, G.W., and Sabatini, D.M. (2016). MERAV: a tool for comparing gene expression across human tissues and cell types. Nucleic Acids Res. *44*, D560–D566. https://doi.org/10.1093/nar/gkv1337.

59. Chanrion, M., Negre, V., Fontaine, H., Salvetat, N., Bibeau, F., Mac Grogan, G., Mauriac, L., Katsaros, D., Molina, F., Theillet, C., and Darbon, J.M. (2008). A gene expression signature that can predict the recurrence of tamoxifen-treated primary breast cancer. Clin. Cancer Res. *14*, 1744–1752. https://doi.org/10.1158/1078-0432.CCR-07-1833.

60. Samson, S.C., Khan, A.M., and Mendoza, M.C. (2022). ERK signaling for cell migration and invasion. Front. Mol. Biosci. *9*, 998475. https://doi.org/10.3389/fmolb.2022.998475.

61. Tsai, P.J., Lai, Y.H., Manne, R.K., Tsai, Y.S., Sarbassov, D., and Lin, H.K. (2022). Akt: a key transducer in cancer. J. Biomed. Sci. *29*, 76. https://doi.org/10.1186/s12929-022-00860-9.

62. Prevete, N., Liotti, F., Illiano, A., Amoresano, A., Pucci, P., de Paulis, A., and Melillo, R.M. (2017). Formyl peptide receptor 1 suppresses gastric cancer angiogenesis and growth by exploiting inflammation resolution pathways. OncoImmunology *6*, e1293213. https://doi.org/10.1080/2162402X.2017.1293213.

63. Snapkov, I., Öqvist, C.O., Figenschau, Y., Kogner, P., Johnsen, J.I., and Sveinbjørnsson, B. (2016). The role of formyl peptide receptor 1 (FPR1) in neuroblastoma tumorigenesis. BMC Cancer *16*, 490. https://doi.org/10.1186/s12885-016-2545-1.

64. Lee, H.Y., Jeong, Y.S., Lee, M., Kweon, H.S., Huh, Y.H., Park, J.S., Hwang, J.E., Kim, K., and Bae, Y.S. (2018). Intracellular formyl peptide receptor regulates naive CD4 T cell migration. Biochem. Biophys. Res. Commun. *497*, 226–232. https://doi.org/10.1016/j.bbrc.2018.02.060.

65. Banh, R.S., Biancur, D.E., Yamamoto, K., Sohn, A.S.W., Walters, B., Kuljanin, M., Gikandi, A., Wang, H., Mancias, J.D., Schneider, R.J., et al. (2020). Neurons release serine to support mRNA translation in pancreatic cancer. Cell *183*, 1202–1218.e25. https://doi.org/10.1016/j.cell.2020.10.016.

66. Leslie, J., Millar, B.J., Del Carpio Pons, A., Burgoyne, R.A., Frost, J.D., Barksby, B.S., Luli, S., Scott, J., Simpson, A.J., Gauldie, J., et al. (2020). FPR-1 is an important regulator of neutrophil recruitment and a tissue-specific driver of pulmonary fibrosis. JCI Insight *5*, e125937. https://doi.org/10.1172/jci.insight.125937.

67. Ferraro, G.B., Ali, A., Luengo, A., Kodack, D.P., Deik, A., Abbott, K.L., Bezwada, D., Blanc, L., Prideaux, B., Jin, X., et al. (2021). Fatty acid synthesis is required for breast cancer brain metastasis. Nat. Can. *2*, 414–428. https://doi.org/10.1038/s43018-021-00183-y.

68. Vareslija, D., Priedigkeit, N., Fagan, A., Purcell, S., Cosgrove, N., O'Halloran, P.J., Ward, E., Cocchiglia, S., Hartmaier, R., Castro, C.A., et al. (2019). Transcriptome characterization of matched primary breast and brain metastatic tumors to detect novel actionable targets. J. Natl. Cancer Inst. *111*, 388–398. https://doi.org/10.1093/jnci/djy110.

69. Morscher, R.J., Ducker, G.S., Li, S.H.J., Mayer, J.A., Gitai, Z., Sperl, W., and Rabinowitz, J.D. (2018). Mitochondrial translation requires folate-dependent tRNA methylation. Nature *554*, 128–132. https://doi.org/10.1038/nature25460.

70. Rossi, M., Altea-Manzano, P., Demicco, M., Doglioni, G., Bornes, L., Fukano, M., Vandekeere, A., Cuadros, A.M., Fernández-García, J., Riera-Domingo, C., et al. (2022). PHGDH heterogeneity potentiates cancer cell dissemination and metastasis. Nature *605*, 747–753. https://doi.org/10.1038/s41586-022-04758-2.

71. Chaneton, B., Hillmann, P., Zheng, L., Martin, A.C.L., Maddocks, O.D.K., Chokkathukalam, A., Coyle, J.E., Jankevics, A., Holding, F.P., Vousden, K.H., et al. (2012). Serine is a natural ligand and allosteric activator of pyruvate kinase M2. Nature *491*, 458–462. https://doi.org/10.1038/nature11540.

72. Ye, J., Mancuso, A., Tong, X., Ward, P.S., Fan, J., Rabinowitz, J.D., and Thompson, C.B. (2012). Pyruvate kinase M2 promotes de novo serine synthesis to sustain mTORC1 activity and cell proliferation. Proc. Natl. Acad. Sci. USA *109*, 6904–6909. https://doi.org/10.1073/pnas.1204176109.

73. Dhayade, S., Pietzke, M., Wiesheu, R., Tait-Mulder, J., Athineos, D., Sumpton, D., Coffelt, S., Blyth, K., and Vazquez, A. (2020). Impact of formate supplementation on body weight and plasma amino acids. Nutrients *12*, 2181. https://doi.org/10.3390/nu12082181.

74. Ron-Harel, N., Notarangelo, G., Ghergurovich, J.M., Paulo, J.A., Sage, P.T., Santos, D., Satterstrom, F.K., Gygi, S.P., Rabinowitz, J.D., Sharpe, A.H., and Haigis, M.C. (2018). Defective respiration and one-carbon metabolism contribute to impaired naive T cell activation in aged mice. Proc. Natl. Acad. Sci. USA *115*, 13347–13352. https://doi.org/10.1073/pnas.1804149115.

75. Sugiura, A., Andrejeva, G., Voss, K., Heintzman, D.R., Xu, X., Madden, M.Z., Ye, X., Beier, K.L., Chowdhury, N.U., Wolf, M.M., et al. (2022). MTHFD2 is a metabolic checkpoint controlling effector and regulatory T cell fate and function. Immunity *55*, 65–81.e9. https://doi.org/10.1016/j.immuni.2021.10.011.

76. Ron-Harel, N., Santos, D., Ghergurovich, J.M., Sage, P.T., Reddy, A., Lovitch, S.B., Dephoure, N., Satterstrom, F.K., Sheffer, M., Spinelli, J.B., et al. (2016). Mitochondrial biogenesis and proteome remodeling promote one-carbon metabolism for T cell activation. Cell Metabol. *24*, 104–117. https://doi.org/10.1016/j.cmet.2016.06.007.

77. Ma, E.H., Bantug, G., Griss, T., Condotta, S., Johnson, R.M., Samborska, B., Mainolfi, N., Suri, V., Guak, H., Balmer, M.L., et al. (2017). Serine is an essential metabolite for effector T cell expansion. Cell Metabol. *25*, 345–357. https://doi.org/10.1016/j.cmet.2016.12.011.

78. Vacchelli, E., Ma, Y., Baracco, E.E., Sistigu, A., Enot, D.P., Pietrocola, F., Yang, H., Adjemian, S., Chaba, K., Semeraro, M., et al. (2015). Chemotherapy-induced antitumor immunity requires formyl peptide receptor 1. Science *350*, 972–978. https://doi.org/10.1126/science.aad0779.

79. Gelderman, K.A., Hultqvist, M., Holmberg, J., Olofsson, P., and Holmdahl, R. (2006). T cell surface redox levels determine T cell reactivity and arthritis susceptibility. Proc. Natl. Acad. Sci. USA *103*, 12831–12836. https://doi.org/10.1073/pnas.0604571103.

80. Chen, X., Song, M., Zhang, B., and Zhang, Y. (2016). Reactive oxygen species regulate T cell immune response in the tumor microenvironment. Oxid. Med. Cell. Longev. *2016*, 1580967. https://doi.org/10.1155/2016/1580967.

81. Pongnopparat, T., Tingley, G., Gao, Y., Brosnan, J.T., Brosnan, M.E., and Christian, S.L. (2021). Oncogenic Ras expression increases cellular formate production. Amino Acids *53*, 1589–1595. https://doi.org/10.1007/s00726-021-03078-5.

82. Ye, R.D., Boulay, F., Wang, J.M., Dahlgren, C., Gerard, C., Parmentier, M., Serhan, C.N., and Murphy, P.M. (2009). International union of basic and clinical pharmacology. LXXIII. Nomenclature for the formyl peptide receptor (FPR) family. Pharmacol. Rev. *61*, 119–161. https://doi.org/10.1124/pr.109.001578.

83. Kim, J.M., Seok, O.H., Ju, S., Heo, J.E., Yeom, J., Kim, D.S., Yoo, J.Y., Varshavsky, A., Lee, C., and Hwang, C.S. (2018). Formyl-methionine as

an N-degron of a eukaryotic N-end rule pathway. Science *362*, eaat0174. https://doi.org/10.1126/science.aat0174.

84. Adams, R.W., Holroyd, C.M., Aguilar, J.A., Nilsson, M., and Morris, G.A. (2013). "Perfecting" WATERGATE: clean proton NMR spectra from aqueous solution. Chem. Commun. *49*, 358–360. https://doi.org/10.1039/c2cc37579f.

85. Labun, K., Montague, T.G., Krause, M., Torres Cleuren, Y.N., Tjeldnes, H., and Valen, E. (2019). CHOPCHOP v3: expanding the CRISPR web toolbox beyond genome editing. Nucleic Acids Res. *47*, W171–W174. https://doi.org/10.1093/nar/gkz365.

86. Cong, L., Ran, F.A., Cox, D., Lin, S., Barretto, R., Habib, N., Hsu, P.D., Wu, X., Jiang, W., Marraffini, L.A., and Zhang, F. (2013). Multiplex genome engineering using CRISPR/Cas systems. Science *339*, 819–823. https://doi.org/10.1126/science.1231143.

87. Nagy, Z.P., Dozortsev, D., Diamond, M., Rienzi, L., Ubaldi, F., Abdelmassih, R., and Greco, E. (2003). Pronuclear morphology evaluation with subsequent evaluation of embryo morphology significantly increases implantation rates. Fertil. Steril. *80*, 67–74. https://doi.org/10.1016/s0015-0282(03)00569-7.

88. Sansom, O.J., Reed, K.R., Hayes, A.J., Ireland, H., Brinkmann, H., Newton, I.P., Batlle, E., Simon-Assmann, P., Clevers, H., Nathke, I.S., et al. (2004). Loss of Apc in vivo immediately perturbs Wnt signaling, differentiation, and migration. Genes Dev. *18*, 1385–1390. https://doi.org/10.1101/gad.287404.

STAR★METHODS

KEY RESOURCES TABLE

REAGENT or RESOURCE	SOURCE	IDENTIFIER
Antibodies		
Rabbit anti-ALDH1L2	ATLAS Antibodies	Cat#: HPA039481; RRID:AB_10795465
Rabbit anti-AKT	Cell Signaling	Cat#:9272; RRID:AB_329827
Rabbit anti-phospho-AKT (S473)	Cell Signaling	Cat#:9271; RRID:AB_329825
Rabbit anti-ERK1/2	Cell Signaling	Cat#:9102; RRID:AB_330744
Rabbit anti-phospho-ERK1/2 (T202/T204) (D13.14.4E)	Cell Signaling	Cat#:4370; RRID:AB_2315112
Rabbit anti-Actin	Abcam	Cat#: Ab8827; RRID:AB_2305186
Mouse anti-Vinculin	Santa Cruz	Cat#: Sc-73614, RRID:AB_1131294
Rabbit anti-MT-CO2	Abclonal	Cat#: A17965; RRID:AB_2861767
Rabbit anti-MT-ND1 (EPR13466(2))	abcam	Cat#: ab181848; RRID:AB_2687504
Rabbit Anti-ALDH1L2 (IF)	Thermofisher	Cat#: PA5-58805; RRID:AB_2637841
Rabbit Anti-FPR1	Abcam	Cat#: ab113531; RRID:AB_10862408
Rabbit Anti-ALDH1L2 (IHC)	Invitrogen	Cat#: PA5-48161; RRID:AB_2633619
Rabbit Anti-S100A9 (EPR22332-75) (IHC)	Abcam	Cat#: ab242945; RRID:AB_2876886
Rabbit Anti-Ki67 (IHC) (SP6)	Abcam	Cat#: ab16667; RRID:AB_302459
Rabbit Anti-Phospho-Histone gammaH2A.X (SER139) (20E3)	Cell Signaling	Cat#: 9718; RRID:AB_2118009
Phycoerythrin coupled anti-FPR1 (Flow)	R&D Systems	Cat#: FAB3744P; RRID:AB_2262859
PE-IgG2A control (Flow)	R&D Systems	Cat#: IC003P; RRID:AB_357245
Goat Anti-Rabbit coupled to A488 (IF secondary)	Abcam	Cat#: Ab150077; RRID:AB_2630356
Horse Anti-Rabbit IgG (IHC secondary)	Vector	Cat#: BA-1100; RRID:AB_2336201
Chemicals, peptides, and recombinant proteins		
Culture media DMEM	ThermoFisher	Cat#: 11965092
Culture media MEM	ThermoFisher	Cat#: 11095080
L-Glutamine	Sigma	Cat#: G7513
D-glucose	ThermoFisher	Cat#: A24940
L-Serine	Sigma	Cat#: S4311
L-Glycine	Sigma	Cat#: G7126
Matrigel	Corning	Cat#: 356231
Lipofectamine 2000	Invitrogen	Cat#: 11668-019
jet-PRIME	Polyplus transfection	Cat#: 101000027
Sodium Formate	Sigma	Cat#: 71539
WKYMVm (FPR agonist)	Tocris	Cat#: 1800
N-F-MLP (FPR agonist)	Sigma	Cat#: F3506
BOC-MLF (FPR inhibitor)	MedChem	Cat#: HY103473A
DAPI	BD Pharmigen	Cat#: 564987
OPTIMA Acetonitrile	Fisher Scientific	Cat#: 10055454
2,3,3-d_3 serine	Cambridge Isotopes	Cat#: DLM-582
OPTIMA Methanol	Fisher Scientific	Cat#: 10767665
OPTIMA Water	Fisher Scientific	Cat#: 10505904
3-nitrophenylhydrazine	Sigma	Cat#: N21804
EDC	Sigma	Cat#: E1769

(*Continued on next page*)

Continued

REAGENT or RESOURCE	SOURCE	IDENTIFIER
Pyridine	Sigma	Cat#: 270407
beta-mercaptoethanol	Sigma	Cat#: M6250
sodium 2,2-dimethyl-2-silapentane-5-sulfonate (DSS)	Sigma	Cat#: 178837
D2O	Sigma	Cat#: 151882
TriPure	Sigma/Roche	Cat#: 11667165001
Critical commercial assays		
MitoTracker Orange	ThermoFisher	Cat#: M7510
MitoSox Red	ThermoFisher	Cat#: M36008
CellRox Deep Red	ThermoFisher	Cat#: C10422
Cytofix/cytoperm	BD Bioscience	Cat#: 554722
IDT PrimeTime gene expression Master Mix	IDT	Cat#: 1055772
Transwell migration assay Costar	Corning	Cat#: 3422
Matrigel invasion chamber	Corning	Cat#: 344480
fMet ELISA	ElabScience	Cat#: E-EL-0063
Deposited data		
RNA sequencing of patients with matched primary breast and metastatic tumors.	Vareslija,D. et al.[68]	https://github.com/npriedig/jnci_2018 and plotted for ALDH1L2
ALDH1L2, *MTHFD2, SHMT2, MTHFD1L* and *FPR1* expression data in normal and tumor breast tissue	Shaul, Y.D. et al.[58]	http://merav.wi.mit.edu.
FPR1 expression in patients with breast cancer with and without metastatic lesions	Chanrion, M. et al.[59]	NCBI_GEO: GSE9893
TCGA-BH-A18V, TCGA-BH-A1ES, TCGA-BH-A1FE, TCGA-E2-A15A, TCGA-E2-A15E, TCGA-E2-A15K.	Broad institute	https://portal.gdc.cancer.gov
Experimental models: Cell lines		
Human breast cancer cell line: MDA-MB-468	The Francis Crick Institute	RRID:CVCL_0419
Human breast cancer cell line: JIMT-1	The Francis Crick Institute	RRID:CVCL_2077
Human breast cancer cell line: HCC70	The Francis Crick Institute	RRID:CVCL_1270
Human breast cancer cell line: MDA-MB-231	The Francis Crick Institute	RRID:CVCL_0062
Human cell line: HEK293T	The Francis Crick Institute	RRID:CVCL_0063
Mouse breast cancer cell line: 4T1	The Francis Crick Institute	RRID:CVCL_0125
Mouse breast cancer cell line: E0771	The Francis Crick Institute	RRID:CVCL_GR23
Experimental models: Organisms/strains		
Mouse Strains: C57BL/6	The Francis Crick institute	N/A
Mouse Strains: BALB/c	The Francis Crick institute	N/A
Mouse Strains: NOD.C-Prkdc^{SCID} Il2rg^{tm1Wjl}/SzJ (NSG)	The Francis Crick institute	N/A
Mouse Strains: C57BL/6 ALDH1L2 KO	Beatson Institute/Francis Crick institute	N/A
Mouse Strains: MMTV-MYC-Cre	The Francis Crick institute	N/A
Oligonucleotides		
Non-targeting siGenome siRNA pool	Dharmacon	Cat#: D-001206
Non-targeting On-Target siRNA pool	Dharmacon	Cat#: D-001810
siGenome siALDH1L2 smart pool	Dharmacon	Cat#: M-026918
On-Target siMTFMT smart pool	Dharmacon	Cat#: L-009633
On-Target siFPR1 smart pool	Dharmacon	Cat#: L-003667
Primer	Table S1	

(*Continued on next page*)

Continued

REAGENT or RESOURCE	SOURCE	IDENTIFIER
Recombinant DNA		
psPAX2	addgene	Addgene plasmid, 12260
VSV.G	addgene	Addgene plasmid, 14888
pCDNA3.1-ALDH1L2	This paper	N/A
pX330-U6-Chimeric_BB-CBh-hSpCas9	Gift from Feng Zhang	Addgene plasmid # 42230 RRID:Addgene_42230
pGFP-C-shALDH1L2	OriGene	TL314843V
pLV-Puro- CMV>hALDH1L2 (VB211128-1010ftp)	This paper	N/A
pLV[Exp]-Puro-CMV>mAldh1l2:P2A:EGFP (VB210527-1256nfw)	This paper	N/A
Software and algorithms		
FlowJo (10.7.2)	FlowJo BD	https://www.flowjo.com
QuantoStudio 3 system	Applied Biosystems	N/A
Fiji	N/A	https://imagej.net/software/fiji/downloads
Bruker pulse program *zgesgppe*	Adams, R.W. et al.[84]	N/A
Chenomx NMR Suite	Chenomx	N/A
TraceFinder	Thermofisher	N/A
Xcalibur	Thermofisher	N/A
gRNA design tool	Labun, K. et al.[85]	https://chopchop.cbu.uib.no
Other		
Waters Acquity BEH C18 column (2.1 × 100mm, 1.7um)	Waters	Cat#: 186002352
SeQuant ZIC-pHILIC column (2.1 3 150 mm, 5 mm)	Merck	Cat#: 1504480001
Mouse Control diet	TestDiet	T-5BQS-1816652-203
Mouse Serine/glycine free diet	TestDiet	T-5BQT-1816653-203

RESOURCE AVAILABILITY

Lead contact

Inquiries about reagents, methods and data availability should be directed to and will be fulfilled by the lead contact, Dr. Karen Vousden (Karen.vousden@crick.ac.uk).

Materials availability

All stable reagents generated in this study are available from the lead contact with a completed transfer agreement.

Data and code availability

- Original data are available from the lead contact on request.
- This paper does not report original code.
- Any additional information required to reanalyze the data is available from the lead contact on request.

EXPERIMENTAL MODEL AND SUBJECT PARTICIPANT DETAILS

Cancer cells

All cell lines were obtained from the Francis Crick Institute Cell Services Science Technology Platform, which ensures various quality controls such as mycoplasma testing, STR profiling and species validation. All cell lines were kept in DMEM (ThermoFisher, 11965092) supplemented with 10% FBS and penicillin-streptomycin at 37°C in humidified atmosphere of 5% CO_2. Serine and glycine starvation media was formulated with MEM (ThermoFisher, 11095080) supplemented with 2 mM L-glutamine, 20 mM D-glucose and MEM vitamins to recapitulate DMEM lacking serine and glycine while control media was supplemented with 400 μM L-serine and glycine.

Animals

All experiments were conducted in compliance with the UK Home Office-approved project licences and personal licences (Animals Scientific Procedures Act 1986) and within institutional welfare guidelines of the Francis Crick Institute or of the CRUK Beatson Institute (reviewed and approved by the University of Glasgow and UK Home Office). Mice (3–5 per cage) had *ad libitum* access to food and water and were kept in a 12h day/night cycle (7:00 to 19:00) in rooms at 21°C and 55% humidity. Mice were acclimatized to their environment for at least one week prior to experimentation. Mice used in the experiments were randomly assigned to experimental groups. BALB/c, C57BL/6 and NOD.C-Prkdc^{SCID} Il2rg^{tm1Wjl}/SzJ (NSG) and MMTV-MYC-CRE were obtained from the in-house breeding facility.

METHOD DETAILS

Tumor mouse models

In Figures 1E–1H, S1F, 3G, and S3G female BALB/c mice in between 8 and 12 weeks old received a 50μL injection of 1x10^5 4T1 cells resuspended in PBS-30% Matrigel in the mammary fat pad under isoflurane anesthesia. Tumors were not resected, and mouse weights were monitored once a week. Mice were transferred to experimental diets 3 days after injection. The experimental diets used are control diet and serine glycine free diet (SGF diet). Briefly, the control diet contains all essential amino acids as well as serine, glycine, glutamine, arginine, cystine and tyrosine. The SGF diet is the same as the control diet but lacking serine and glycine, which are compensated by a proportionally increased level of the other amino acids to reach the same total amino acid content (Testdiet). MMTV-MYC mice were switched to either control diet or -SG diet in between 4 and 6 weeks of age.

In Figures 2C, 2D, and S2F mice were exposed to gamma-irradiation of 0.423 Gy/min from ^{137}Cs sources. Mice were sacrificed 72h after irradiation and guts were flushed and fixed in Neutral buffered Formalin.

In Figures 6B–6H, S6F, and S6G, female NOD.C-Prkdc^{SCID} Il2rg^{tm1Wjl}/SzJ (NSG) mice between 8 and 12 weeks old received a 50μL injection of 5x10^6 MDA-MB-468 cells resuspended in PBS-30% matrigel into the mammary fat pad under isoflurane anesthesia. Tumors were not resected and mouse weights were monitored once a week.

In Figures 6I–6K and S6H, female NOD.C-Prkdc^{SCID} Il2rg^{tm1Wjl}/SzJ (NSG) mice between 8 and 12 weeks old received a 50μL injection of 5x10^6 MDA-MB-231 cells resuspended in PBS-30% matrigel in the mammary fat pad under isoflurane anesthesia. Tumors were not resected and mouse weights were monitored once a week.

In Figures 7A–7F, 7K, S7C, S7G–S7O, and S6E (right), female BALB/c mice between 8 and 12 weeks received a 50μL injection of 0.5x10^5 4T1 cells resuspended in PBS-30% matrigel in the mammary fat pad under isoflurane anesthesia. Tumors were not resected and mouse weights were monitored once a week.

In Figures 7I, 7J and 7L, 2.5x10^5 4T1 cells resuspended in 100μL of saline were injected in the tail vein of female BALB/c mice and sacrificed 18 days after injection.

In Figures 7G, 7H, and S7D–S7F, female C57BL/6 mice between 8 and 12 weeks received a 50μL injection of 0.5x10^5 E0771 cells resuspended in PBS-30% matrigel in the mammary fat pad under isoflurane anesthesia. Tumors were not resected and mouse weights were monitored once a week.

For all mouse experiments: Blood was collected through cardiac puncture into EDTA coated tubes that were spun at 2000g for 15 min at 4°C to generate plasma. Tumors were harvested either at equivalent sizes (tumor size matched) or at the same endpoint in time independently of size (time-matched) as specified in the Figure legends. Tumor interstitial fluid (TIF) was collected by placing the tumors in Spin-x filter tubes (Costar 8170) and centrifuged sequentially at 100g, 400g and 1500g for 10 min at 4°C. Tumors were then split into two, the first part snap frozen in liquid nitrogen for LC-MS and Western blot analysis and the second part fixed in neutral buffered formalin for immunochemistry. Lungs were collected and directly fixed into neutral buffered formalin for immunochemistry. For analysis of lung metastasis, 2 sections separated by 70μm were stained with H&E.

Generation of ALDH1L2 knock-out mice

For the generation of a mouse line carrying an *Aldh1l2* KO allele, a mutation was introduced into the mouse *Aldh1l2* gene (Ensembl ID: ENSMUSG00000020256) using genome editing. The resultant mutation was a 72bp deletion in exon 4 (Ensembl ID: ENSMUSE00001206021 in Genome Assembly GRCm39) of the *Aldh1l2* transcript *Aldh1l2-201* (Ensembl ID: ENSMUST00000020497.14). The mutation removes the last 50bp of exon 4 and spans the splice donor site at the boundary of intron 4–5. A guide RNA directed to exon 4 of murine *Aldh1l2* (5′ CGTCAAGCCCAATGACACAGTGG-3′) was identified using the CHOPCHOP CRISPR gRNA design tool (https://chopchop.cbu.uib.no/).[85] These sequences were cloned into pX330 (expressing Cas9 and gRNA)[86] and the resultant vectors transfected into HM1 mouse embryonic stem cells with a passenger PGK-PURO plasmid. pX330-U6-Chimeric_BB-CBh-hSpCas9 was a gift from Feng Zhang (Addgene plasmid # 42230; http://n2t.net/addgene:42230; RRID:Addgene_42230). Following selection under puromycin, surviving ESC were re-plated at low density and individual colonies picked and expanded. To identify clones carrying potential CRISPR-generated mutations, genomic DNA from individual colonies was isolated then screened by PCR (GoTaq; Promega, Madison, Wisconsin, USA) and the Surveyor Mutation Detection Kit (Integrated DNA Technologies, Coralville, Iowa, USA), according to manufacturers' protocols. PCR primers (5′ GCCATTATTGCAAGACTACACATAC-3′ and 5′ CTCTCTTTGAAGAGGAACAAGTCAC-3′) were designed to amplify a 532bp region surrounding the guide sequence in exon 4 of the Aldh1l2 gene, to allow identification and characterisation of CRISPR generated

mutations. Obvious indels were evident following PCR and these were confirmed by Surveyor assay screening. Additional small indels not obvious by PCR screening alone, were also identified using the Surveyor assay. PCR products of the target area from potentially mutated colonies were cloned into a plasmid backbone and sequenced using M13F and M13R primers. Clone CH1-2F carried the 72bp deletion that removed the 3′ end of exon 4 and was anticipated to generate a null allele. Following identification of a clone carrying the modified *Aldh1l2* allele, mouse lines were derived by injection of ES cells into C57BL/6J blastocysts according to standard protocols.[87] After breeding of chimeras, germline offspring were identified by coat color and the presence of the modified allele was confirmed with the *Aldh1l2* primers described above, and confirmation by DNA sequencing.

Cell proliferation

For Figures S1A, S7A, and S7B, $1x10^5$ MDA-MB-468, JIMT-1 and 4T1 cells were seeded in a 6 well plate and media was changed once cells had attached. Cells were trypsinized 24h and 72h after media change, diluted in PBS-EDTA and counted with a CASY Model TT Cell Counter (Innovatis, Roche Applied Science). For Figure 4A, cells were seeded at $3x10^5$ cells in 6 well plates and transfected as described below, 72h after transfection cells were counted as described. For Figure 4B, cells were seeded at $3x10^5$ cells in 6 well plates and transfected as described below. After 24h, cells were counted as a starting reference and media was changed with treatment media containing 0.5mM of N-Acetyl-Cysteine or PBS. After 72h of treatment cell were counted and fold change from starting reference calculated. Graph represents the relative growth fold change.

siRNA transfection and ALDH1L2 overexpression

MDA-MB-468, JIMT-1 or HCC70 were seeded at $4x10^5$ cells in 6 well plates overnight. Cells were then transfected with 10μM of non-targeting siRNA (siGenome control pool #D-001206, ON-target plus control pool #D001810), siALDH1L2 (siGenome Smart pool #M-026918), siMTFMT (ON-target plus Smart pool #L-009633) or siFPR1(ON-target plus smart pool #L-003667) from Dharmacon using Lipofectamine 2000 (11668-019 from Invitrogen) following the manufacturer's instructions. ALDH1L2 transient overexpression in MDA-MB-231 was achieved by transfecting a pCDNA 3.1 plasmid containing the ORF of ALDH1L2 using jet-PRIME reagent (Polyplus transfection).

ALDH1L2 stable depletion and overexpression

ALDH1L2 stable depletion was obtained by infecting MDA-MB-468 cells with lentiviral particles containing shRNA targeted against ALDH1L2 (TL314843V, OriGene). HEK293T cells were transfected with lentiviral plasmids containing ALDH1L2 ORF (pLV-Puro-CMV>hALDH1L2 (VB211128-1010ftp) or Aldh1l2 ORF pLV[Exp]-Puro-CMV>mAldh1l2:P2A:EGFP (VB210527-1256nfw) together with psPAX2 (Addgene, 12260) and VSV.G (Addgene, 14888) using jet-PRIME reagent (Polyplus transfection). After 24h incubation, medium was changed and 48h later, the viral particle containing-medium was filtered (0.45mm) and mixed with polybrene (4 μg/mL, Sigma-Aldrich). The medium containing lentiviruses was incubated with the target cells for 24h. Cells were then selected for 3 weeks in puromycin. OE-ALDH1L2 and equivalent empty vector cells were single cell cloned in 96 well plate on the basis of GFP expression by flow cytometry.

Cell migration and invasion

For cell migration, $2.5x10^4$ MDA-MB-231, $5x10^4$ MDA-MB-468 cells, $5x10^5$ 4T1 cells, $1x10^5$ JIMT-1 cells, $1x10^5$ HCC70 or $1x10^5$ E0771 cells were resuspended in 150μL of serum free media and deposited onto the upper chamber of the Transwell migration assay (Costar 3422 from Corning, 8 micron pore size) for migration or matrigel invasion chamber (344480 form Corning, 8 micron pore size) using medium with 1% serum in the lower chamber. For treatment, cells were pre-treated overnight with either 1mM sodium formate (Sigma), 20μM WKYMVm (#1800 Tocris), 50μM N-F-MLP (F3506, Sigma), or 20μM BOC-MLF (HY103473A MedChem), then cells were resuspended in serum free media containing the treatment. After 20h, cells that remained in the upper chamber were removed with a cotton-tip. Cells that migrated/invaded to the other side of the insert were then fixed in 70% ethanol and stained either with 1/10 000 DAPI (#564987 BD Pharmigen) in ethanol for migration assay or 0.5% crystal Violet for invasion. Cells were then photographed with an Evos microscope from ThermoFisher. For migration assays, data for one replicate well represents the average of the quantification through ImageJ of 3-to-5 images per well taken with an Evos microscope (ThermoFisher).

Liquid chromatography mass spectrometry

For all LC-MS experiments 10% of dialyzed FBS was used in DMEM. For unlabelled fMet detection in Figures 3H, 3I, S3F, and S3I, $4x10^5$ of MDA-MB-468, JIMT-1 and MDA-MB-231 cells were plated in 6-well plates. Duplicate plates were used for cell counting to normalize the LC-MS analysis by cell number. Cells were extracted with 1mL of ice-cold extraction buffer (methanol/acetonitrile/water at a 50/30/20 ratio) per $2x10^6$ cells, vortexed and spun down at 15000 g for 12 min at 4°C. Supernatants were used for LC-MS analysis. Analytes were separated using hydrophilic interaction liquid chromatography with a SeQuant ZIC-pHILIC column (2.1 3 150 mm, 5 mm) (Merck) and detected with high-resolution, accurate-mass mass spectrometry using an Q Exactive Orbitrap from ThermoFisher in line with a Vanquish autosampler and a Vanquish pump (Thermofisher). The elution buffers were acetonitrile for buffer A and 20 mM (NH4)2CO3 and 0.1% NH4OH in H2O for buffer B. A linear gradient was programmed starting from 80% buffer A and ending at 20% buffer A after 20 min, followed by wash (20% buffer A) and re-equilibration (80% buffer A) steps with a flow rate of 300 μL/min. The mass spectrometer was fitted with an electrospray-ionization probe and operated in full-scan and polar-switching

mode with the positive voltage at 3.5 kV and negative voltage at 2.5 kV. For labeling experiments in Figures 3E, 3F, and S3C, $5x10^5$ of MDA-MB-468 and MDA-MB-231 cells were plated in 6-well plates in the experimental media 24h prior to the labeling. Duplicate plates were used for cell counting to normalize the LC-MS analysis by cell number. After 24h in the experimental media, media were replaced by the equivalent media depleted of serine and supplemented with 400μM of labeled $^{2,3,3}D_3$ serine (DLM-582) from Cambridge Isotopes for 4h. Cells were washed with PBS and metabolites were extracted in the plate with the same extraction buffer as described above. After vortexing and centrifugation at 15000 g for 12 min at 4°C, supernatants were used for LC-MS analysis. For the analysis of tumor samples, tissue (10-20 mg/mL of described extraction buffer) was homogenised with hard tissue homogenizing tubes (CK28-R) in a precellys-24 homogenizer (Bertin Technologies) at 6000g for 3 × 30sec and kept at 4°C with a Cryolys (Bertin Technologies). Homogenate was collected and spun at 15000g for 12 min at 4°C and the supernatant collected for LC-MS analysis. For plasma samples, plasma was diluted 20-fold with the same extraction buffer, vortexed and spun at 15000g for 12 min at 4°C. The supernatant was collected for analysis. For tumor interstitial fluid (TIF), tumors were placed in Spin-x filter tubes (Costar 8170) and centrifuged sequentially at 100g, 400g and 1500g for 10 min at 4°C. TIF was then diluted 20-fold in the same extraction buffer, vortexed and spun at 15000g for 12 min at 4°C. LC-MS analysis was described as above and data were analyzed with TraceFinder and Xcalibur from Thermofisher. Normalization was obtained with the presence of internal standard.

Liquid chromatography mass spectrometry, formate detection

The formate detection method was derived from a published protocol for acetate detection and suggested by Prof J. Rabinowitz.[29] This method allows derivatization of formate and column separation without presence of formic acid in the elution buffers. For intracellular formate detection in Figures 1D and S3A by LC-MS, $4x10^5$ cells were plated in 6 well plates. Duplicate plates were used for cell counting to normalize the LC-MS analysis by cell number. For intracellular M+1 labeled formate detection in Figures 3D and S3B, cells were plated in 6-well plates in the experimental media 24h prior to the labeling. Duplicate plates were used for cell counting to normalize the LC-MS analysis by cell number. After 24h in the experimental media, media were replaced by the equivalent media depleted of serine and supplemented 400μM of labeled $^{2,3,3}D_3$ serine (DLM-582) from Cambridge Isotopes for 24 h. Cell pellets were collected and extracted in 1mL of ice-cold extraction buffer (methanol/acetonitrile/water in the 50/30/20 ratio) per $2x10^6$ cells, vortexed and spun down at 15000 g for 12 min at 4°C. Supernatant was then dried in a SpeedVac. Dry samples were resuspended in 200μL of a cold derivatization mix (1/1/3) composed of EDC (11.5 mg/ml in MeOH, #E1769 from Sigma) 3-nitrophenylhydrazine (23.5 mg/mL in MeOH, #N21804 from Sigma) and Pyridine (40μL in 1mL of MeOH) and incubated for 1h at 4°C with 3 cycles of 10min sonication. Samples were then centrifuged at 15000g for 12 min and 50μL of the supernatant was added to 500μL of beta-mercaptoethanol (500μM). Samples were centrifuged again at 15000g for 12 min before being transferred in vials. Analytes were separated using hydrophilic interaction liquid chromatography with a Waters Acquity BEH C18 column (2.1 × 100mm, 1.7μm) at 60°C. The elution buffers were water for buffer A and methanol for buffer B. Gradient started from 10% of buffer B and was programmed as following: 0-1min:10% B; 2-4min 15 to 30% B; 4-5min 20 to 100%; 5-7min 100% B; 7-7.2min 100%–15% B at a flow rate of 0.2 mL/min. Analytes were detected with high-resolution, accurate-mass mass spectrometry in negative mode using a Q Exactive orbitrap from Thermofisher in line with a Vanquish autosampler and pump (Thermofisher).

For the analysis of formate in tumor samples, tissue (~20 mg/mL of described extraction buffer) was homogenised with hard tissue homogenizing tubes (CK28-R) in a precellys-24 homogenizer (Bertin Technologies) at 6000g for 3 × 30sec and kept at 4°C with a Cryolys (Bertin Technologies). Homogenate was collected and spun at 15000g for 12 min at 4°C and the supernatant was dried by SpeedVac before being derivatized as described above. For plasma and TIF samples, 5μL of sample was directly diluted in 100μL of derivatization buffer and incubated for 1h at 4°C with 3 cycles of 10min sonication. Samples were then centrifuged at 15000g for 12 min and 20μL of the supernatant was added to 200μL of beta-mercaptoethanol (500μM). Samples were centrifuged again at 15000g for 12 min before being transferred in vials. LC-MS analysis was described as above and data were analyzed with TraceFinder and Xcalibur from Thermofisher.

Nuclear magnetic resonance

NMR was used to measure formate in the supernatant of cells as represented in Figures 1C, 3A, 3B, and 3C. 160 μL of supernatant was collected for NMR analysis and cells were counted as already described to allow normalization to cell number. NMR was used to measure formate in plasma and TIF as shown in Figures 1E, 6A, 6E, S6D, S7G, and S7I, plasma and TIF were collected and diluted 10x in PBS. NMR was used to A solution of 10 mM DSS (sodium 2,2-dimethyl-2-silapentane-5-sulfonate from Sigma) diluted in D_20 was added to the samples to obtain a final concentration of 1 mM DSS. NMR spectra were acquired at 25°C with a Bruker Avance III HD instrument with a nominal ^1H frequency of 700 MHz using 3 mm tubes in a 5 mm CPTCI cryoprobe. For ^1H 1D profiling spectra the Bruker pulse program *zgesgppe* for excitation sculpting with pure echo[84] was used with 20 ppm sweep width, 1s relaxation delay and 4s acquisition time. Typically, 128 or 256 (for plasma and TIF) transients were acquired. Data were processed and analyzed using *Chenomx NMR Suite* (Chenomx, Edmonton, Canada). Free induction decays were zero-filled, apodized with exponential multiplication (line-broadening factor LB = 1 Hz), Fourier transformed and the resulting spectra were then phase corrected before baseline correction, all in the Processor component of the Chenomx software. Formate quantitation was performed based on the chemical shift reference (DSS) assumed to be at 0.1 mM concentration and with line width adjusted to obtain a good fit to the Chenomx library spectra for multiple metabolites in the spectrum. Absolute quantification in Figures 3D and S6G were obtained with a 6 point standard curve spikes into plasma or TIF.

Western blot and ELISA

For Figures S2A, S2B, S2E, S3H, S4E, S6E and S7M, cells were lysed with RIPA-buffer (Millipore) supplemented with phosphatase inhibitor cocktail (ThermoFisher Scientific) and complete protease inhibitors (Roche) after pelleting. For Figures S6B and 7F, 20mg of tissue was lysed with RIPA-buffer in Hard tissue homogenizing tubes (CK28-R) in a precellys-24 homogenizer (Bertin Technologies) at 6000g for 3 × 30 s maintained at 4°C with a Cryolis (Bertin Technologies). Then, proteins were separated using precast 4–12% Bis-Tris gels (Invitrogen) and transferred to nitrocellulose by dry-transfer (iBlot, ThermoFisher Scientific). Membranes were probed with the following primary antibodies: ALDH1L2 (HPA039481) form Atlas Antibodies; p-AKT (#9271), AKT (#9272), p-ERK1/2 (#4370) and ERK1/2 (#9102) from Cell Signaling; Actin (ab8226), MT-ND1 (ab181848) from Abcam; MT-CO2 (A17965) from Abclonal and Vinculin (sc-73614) from Santa Cruz Biotechnology. All antibodies were used at a dilution of 1:1000 Blot were developed with ECL chemiluminescence kits (Pierce) after incubation with appropriate species-specific horseradish peroxidase-conjugated antibodies. All antibodies were verified and confirmed for species as per the manufacturers' disclosures.

For Figure S3E, $2x10^6$ 293T cells were harvested and pelleted. Pellet was then resuspended in PBS and three freeze/thaw cycles were performed before centrifugation at 10000g for 20 min at 4°C. ELISA was then performed according to manufacturer's instructions (E-EL-0063 from ElabScience).

Immunofluorescence

For immunofluorescence, $2x10^4$ cells were cultured overnight on a coverslip in a 12 well plate and incubated 10min with 250nM of MitoTracker Orange (M7510, ThermoFisher) at 37°C before being fixed with 4% PFA. Cells were permeabilized with 0.1% Triton X-100 and incubated with 1% BSA, 22.52 mg/mL glycine in PBST (PBS+ 0.1% Tween 20) for 60 min to block unspecific binding of the antibodies. Coverslips were then incubated overnight at 4°C with anti-ALDH1L2 (PA-58805, invitrogen) antibody at 1/100 or anti-FPR1 (ab113531). Cells were then incubated with the Alexa Fluor 488 coupled secondary antibody at 1/500 for 1h at room temperature. Coverslips were mounted on slides with Vectashield hardset DAPI (H-1500) containing mounting media. Samples were imaged on a Zeiss Invert710 and pictures generated with ImageJ Fiji.

Histology and immunohistochemistry

For Figures S2F, 7H, 7G, and S7F, tissues were fixed in 10% neutral buffered formalin for 24h. The fixed tissues were processed using Sakura Tissue-Tek VIP 6 AI Tissue Processor and paraffin embedded. 3μm sections were cut on to Plus+Frost positive charged slides (MSS51012BU, Solmedia). For analysis of lung metastasis, 2 sections separated by 70μm were stained with H&E. The slides were baked at 60°C for 1h and then deparaffinized in xylene and rehydrated using a series of graded industrial methylated spirits solutions and distilled water. Heat-mediated antigen retrieval was performed using pH6 citrate buffer for 20 min in a microwave. Endogenous peroxidase blocking was performed by incubating the slides in Bloxall (SP-6000-100, Vector) for 10 min at room temperature. Protein blocking was performed using a blocking buffer of TBS-T, 10% bovine serum albumin (A3294, Sigma-Aldrich), 4% milk for 1h at room temperature. For Figures S2D, 7K, 7L, S7N, and S7O, primary antibody ALDH1L2 (PA5-48161, Invitrogen) was diluted in 1% BSA at a 1:100 dilution and was incubated for 1h at room temperature. For Figure 7D primary antibody S100A9 (ab243108) was diluted in 1% BSA at a 1:15000 dilution and was incubated for 1h at room temperature. Horse anti-rabbit IgG (BA-1100, Vector) was diluted at 1:200 in TBS and incubated for 30 min at room temperature. Slides were incubated with Vectastain Elite ABC kit peroxidase (PK-6100, Vector) for 30 min at room temperature and then incubated with 3,3-diaminobenzidine (DAB) chromatin (SK-4105, Vector) for 10 min at room temperature for visualization. The slides were then counterstained using Harris Haematoxilin and dehydrated, cleared and mounted using Sakura Tissue-Tek Prisma auto stainer. For Figures 2C, 2D, and S2F, histology and immunohistochemistry were performed as described previously.[88] Primary antibodies used were anti-Ki67 (Abcam, ab16667) and γH2A.X (Cell Signaling Technology, #9718). For Figures S7C and S7O, Ki67 staining was performed as automated immunohistochemistry staining on the Ventana Discovery Ultra Slide Preparation System (Roche). Antigen retrieval was obtained with Cell Conditioning 1 (CC1) from Ventana Medical Systems. Primary antibody Ki67 (Abcam, ab15580) was diluted 1/1000 in Discovery Ab Diluent (Roche 05266319001). All primary antibodies were incubated for 60 min. Slides were scanned with Zeiss AxioScan Z1 and images generated and quantified with positive cell detection algorithm on QuPath.

Flow cytometry

For Figures 2B and S2C, $4x10^5$ cells were plated on a 6 well plate and transfected with ALDH1L2 siRNA as described above. After 48h cells were incubated with either 5μM of MitoSox Red mitochondrial superoxide indicator (M36008) from ThermoFisher Scientific for 10 min at 37°C or 5μM of CellRox Deep Red (C10422) from ThermoFisher Scientific for 30 min at 37°C. Cells were washed with PBS-1mM EDTA-2.5% FBS and filtered into FACS tubes. Samples were run on a FACS Aria with data acquired with FACSdiva and analyzed with FlowJo (10.7.2). For Figure 3F, $4x10^5$ cells were plated in a 6 well plate and left overnight to attach. Cells were then pelleted in PBS-1mM EDTA-2.5% FBS and fixed with 4% PFA. Cells were first stained with 1/1000 efluor-780 live/dead for 20 min at 4°C. The cells were then permeabilized with BD Cytofic/Cytoperm Kit and stained overnight at 4°C with 10μL of Phycoerythrin coupled anti-FPR1(FAB3744P) or PE-IgG2A control (IC003P) from R&D systems. Cells were washed with PBS-1mM EDTA-2.5% FBS and filtered into FACS tubes. Samples were run on a FACS Aria with data acquired with FACSdiva and analyzed with FlowJo (10.7.2).

RNA extraction and RT-qPCR

Total RNA was extracted using TriPure isolation reagent (Roche) from at least three technical replicates. cDNA was generated using the High-capacity cDNA reverse transcription kit (ThermoFisher) according to manufacturer's instructions. IDT PrimeTime Gene expression master mix (IDT) was used to perform qPCR with the following predesigned primer/probe assay from IDT; *FPR1* (Hs.PT58.19261258), *POLRA* (Hs.PT.39a.19639531), *MTFMT* (HS.PT.58812342). Sequences can be found in Table S1. Data were collected on a QuantStudio 3 system from Applied Biosystems.

Meta-analysis of available databases

For Figures S5D and S6A, expression data in normal tissue and breast cancer patients for *ALDH1L2*, *MTHFD2, SHMT2, MTHFD1L* and *FPR1* was downloaded from http://merav.wi.mit.edu.[58] For Figure S5E, data were downloaded from NCBIGEO: GSE9893.[59] For Figure S6B, *ALDH1L2* expression in human cancer cell lines was obtained from the cancer cell line encyclopedia (CCLE): https://www.cbioportal.org. For Figure 7M, raw count data (.txt file) from RNA sequencing of patients with matched primary breast and metastatic tumors were downloaded from https://github.com/npriedig/jnci_2018 and plotted for *ALDH1L2*.[68] For Figure S7P, data were extracted from the breast cancer TCGA dataset. Patients were removed from the analysis if they had: 1) missing date of birth, or 2) missing survival information, on the basis of no death date, no last follow-up date and no vital status information. For the remaining patients, censoring was defined as either the day of last follow-up or date of death. The event of interest was set to 'vital status', marked as 1 for patients who died prior to last follow-up, and 0 otherwise. To assess the impact of *ALDH1L2* gene expression on breast cancer survival, we evaluated the top and bottom 15% percentile of *ALDH1L2* gene expression in the TCGA dataset (TCGA: https://portal.gdc.cancer.gov), and divided *ALDH1L2* gene expression into 3 categories: low (bottom 15%), very high (top 15%) and mid (median 70%, reference group). Kaplan Meier (KM) survival curves were produced using survival data, counted as the number of days to censoring, analyzed against two categories of *ALDH1L2* gene expression marked as 'very high' (top 15%) and 'low' (remaining 85%). p-value represents the probability that both groups to have the same survival profile. For Figure 7N, *ALDH1L2* expression of the following breast cancer patient samples with matching primary and metastasis RNA expression data were extracted from the TCGA base: TCGA-BH-A18V, TCGA-BH-A1ES, TCGA-BH-A1FE, TCGA-E2-A15A, TCGA-E2-A15E, TCGA-E2-A15K. Expression data was then converted in log2 before being plotted.

QUANTIFICATION AND STATISTICAL ANALYSIS

All statistical analyses were performed using GraphPad Prism 8 software. Unpaired Student t-test was performed to compare two groups to each other. If the variance, determined by the F test, between the two groups was unequal, a Welch's correction was applied. For multiple comparison, a one-way ANOVA was used. If the variance between groups, determined by the Brown-Forsythe test, was unequal, a Brown-Forsythe and Welch correction was applied. p value below 0.05 was considered statistically significant. Significance is indicated as follows: *$p < 0.05$, **$p < 0.01$, ***$p < 0.001$, ****$p < 0.0001$, ns: no significance. Statistical test is mentioned in each Figure legend. All measurements were taken from distinct samples, as noted in the Figure legends, and no data were excluded. Sample sizes were based in standard protocols in the field, metabolic data were assigned in a random order before analysis by LC-MS, mice were randomly assigned to a treatment and mouse experiments were blinded to the person performing metabolomic or immunohistology analysis.